

Post-Elastic Response of Structures to Synthetic Ground Motions

By Paolo Bazzurro¹, Brian Sjoberg¹, and Nicolas Luco¹

Abstract

When real recordings for a specific earthquake scenario are scarce, engineers often use synthetic records generated by seismologists as input to nonlinear dynamic analyses of both existing and new structures. This practice has sometimes generated concerns among practitioners regarding the accuracy of the nonlinear response obtained using simulated ground motions. This article presents a case study where the issue of structural response accuracy is investigated for seven simulation techniques whose derived structural responses are statistically compared against the “correct” answer provided by real accelerograms. The example involves seven suites of synthetic records that emulate real ground motions recorded at 20 stations located within 20km from the Northridge fault rupture. The results show that six out of seven simulation methods appear to be biased, especially in the short period range, both in the linear elastic and in the nonlinear post-elastic regimes. The tendency of these synthetic records is to create linear responses that are more severe than those from the real counterparts in the short period range. This tendency is reversed in the nonlinear regime where responses from synthetic records in the same short period range tend to be less severe than those from real accelerograms. Synthetic records seem to be especially benign in relatively weak and stiff structures. Simulated records also tend to produce nonlinear responses that are less variable than those caused by real records in the short period range and more variable in the long period range. This discrepancy should be taken into consideration when using synthetic records for assessing, for example, the safety of a structure against collapse. The results mentioned above were found to be stable to the sensitivity performed on different parameters and assumptions of the analyses. It should be emphasized, however, that these conclusions were found from one case study only and their validity may not apply to other cases or to different simulation techniques. More research is needed to establish the range of applicability of these findings.

1.0 Introduction

Consideration of the post-elastic dynamic response of structures is of fundamental importance in earthquake engineering as most buildings are expected to deform beyond their linear elastic limit during intense ground shaking. In recent years, the computation of a structure's dynamic inelastic response to an earthquake event has been done more frequently than ever before via time-history analysis. Ideally, the input ground motions to such analyses are past recordings of earthquakes with similar characteristics (e.g. magnitude, distance, and fault mechanism) to the earthquake scenarios that dominate the seismic hazard at the structure's site. Unfortunately, real recordings of ground motions with suitable characteristics are often scarce or non-existent. This shortage of adequate ground motions has led to the engineering practice of modifying real accelerograms to meet a prescribed ground shaking intensity level or target elastic response spectrum. Techniques often used involve scaling the amplitude of real accelerograms or adjusting their frequency content to match a target spectrum. The alternative to modifying real accelerograms is to use completely synthetic (also referred to as simulated) earthquake

¹ AIR Worldwide Co., 388 Market Street, Suite 610, San Francisco, CA 94111

time-histories, which are founded upon the basic physical principles controlling fault rupture and seismic wave propagation from source to site. This study is concerned with this latter alternative and the effect that using simulated time-histories may have on seismic performance assessment.

Like the practice of modifying real accelerograms by amplitude scaling or spectrum matching, the use of synthetic time histories has caused concern amongst some engineers. We interpret these concerns here as being twofold:

- Simulated ground motion records may not produce, on average, the same nonlinear structural response as real ground motion recordings with the same nominal intensity. If there were a systematic deviation (sometimes referred to here as bias for conciseness sake), then engineers may either not use simulated records or account for the bias in their seismic performance analyses when using synthetic rather than real recordings.
- The record-to-record variability of nonlinear structural response produced by synthetic and real records with otherwise similar characteristics may not be comparable. This variability has an impact on how likely extreme values of structural responses are and, therefore, on the estimates of probability of occurrence of extreme events such as collapse.

We investigate these issues by comparing the nonlinear response statistics of nonlinear single-degree-of-freedom (SDOF) oscillators of different structural periods and yield strengths to both real and simulated records. In particular, we consider one real ground motion dataset, whose response statistics are used as a benchmark, and seven synthetic ground motion datasets. A direct comparison of response statistics is legitimate because the seven simulated datasets were developed to match the same earthquake and site conditions of the real recordings.

2.0 Description of the Synthetic and Real Ground Motion Datasets

The simulated ground motion time histories that are used here were originally developed as part of the PEER K201 project entitled “*Ground Motions for the Treasure Island National Geotechnical Experimental Site*”. The K201 project compares elastic response spectral values from simulated ground motions with those from real recordings of past earthquakes for the purpose of validating various ground motion simulation methods. The following seismologists developed the synthetic time histories used in the K201 project and in this project:

1. Igor A. Beresnev²;
2. Douglas Dreger³;
3. Alexander A. Gusev⁴ *et al.*;

² Associate Professor of Geophysics, Iowa State University, Ames, Iowa.

³ Associate Professor of Geophysics, University of California, Berkeley, California.

⁴ Head, Laboratory of Seismology, Institute of Volcanic Geology and Geochemistry, Petropavlovsk-Kamchatsky, Russia.

4. Lawrence Hutchings⁵ *et al.* (denoted as LLNL hereafter);
5. Walter Silva⁶;
6. Paul G. Somerville⁷ *et al.* (denoted as URS hereafter);
7. Yuehua Zeng⁸.

Note that both Dreger and Zeng, based on the preliminary results from this study, updated their dataset of synthetic motions with respect to those used in the K201 Project.

The seven datasets contain simulated time histories that are intended to reproduce those generated by the M6.7 1994 Northridge earthquake at 20 near-field stations that ranged in distance from 5.2km to 19.1km (Table 1). An eighth dataset contains the real recordings at the same 20 stations. Here we used only the horizontal components, whereas the vertical components are neglected. Table 2 summarizes the details about the time histories provided by each seismologist. In four (i.e., Dreger, Gusev, URS, and Zeng) out of seven cases, the simulated recordings consisted of both horizontal component time histories for each of the 20 stations. Two horizontal components were also available in the LLNL dataset but only for 12 stations. Beresnev and Silva did not provide separate horizontal components but rather a single “average” time history of horizontal ground motion at each one of the 20 stations. Therefore, a total of 224 synthetic horizontal ground motion time histories were considered as input to the nonlinear dynamic analyses carried out in this study.

As discussed above, the available suite of simulated input time histories is partially incomplete and somewhat heterogeneous. Despite this drawback, we intended as much as possible to enable a legitimate comparison of nonlinear responses that encompasses all seven datasets. To achieve this goal, for five datasets (i.e., Dreger, Gusev, LLNL, URS, and Zeng) we computed the spectral responses for the two horizontal components at each station and combined them into an “average” spectral response. For the remaining two datasets (i.e., Beresnev and Silva) we computed the responses to the “average” time history provided by the developers. In the former case the average response was calculated using two different averaging methods, the geometric mean and the root-mean-square (rms) value. For nearly all subsequent comparative analyses, the rms value was used to describe the station-by-station structural response for each synthetic ground motion dataset that contained separate components. This alternative was selected because it is consistent with the methodology used in the generation of the average ground motion time histories. The geometric mean value was used only secondarily to assess whether the trends in the nonlinear responses observed for each modeler would be dependent on the particular component averaging method. The comparison of the results obtained with the two averaging methods is reported in Section 4.2.

⁵ Lawrence Livermore National Laboratory, Livermore, California.

⁶ Pacific Engineering & Analysis, El Cerrito, California.

⁷ URS Corporation, Pasadena, California.

⁸ Research Associate Professor, Mackay School of Earth and Environmental Sciences, University of Nevada, Reno, Nevada.

With reference to Table 1, the usable bandwidth of the *real records* exceeded 0.1 – 4.0 seconds for all but three recording stations (KAT, LA0, PAR), since the highpass (HP) and lowpass (LP) corner frequencies of the causal Butterworth filter used to process such records were less than 0.2 Hz and greater than 12.5 Hz, respectively⁹. The usable bandwidth of a record processed using a causal Butterworth 4-pole filter, such as that used for these records, is recommended to be between 1/1.25 times the LP frequency and 1.25 times the HP frequency due to the significant reduction imposed by the filter in the neighborhood of the corner frequencies (Abrahamson and Silva, 1997, PEER documentation – <http://peer.berkeley.edu/smcat/process.html>). Therefore, for records filtered with a high-pass frequency of 0.2 Hz, caution must be exercised when investigating the response of a structure with a period greater than $1/(0.2 \text{ Hz} * 1.25) = 4.0\text{s}$. The reader should also keep in mind that the recommendation on the usable bandwidth reported above (and below for the synthetic records) was provided with no specific attention to the use of such records as input to structural *nonlinear* dynamic analyses. The effective structural period of vibration may significantly lengthen outside the suggested usable bandwidth of the record as the damage severity progresses. In this study we have not made any attempt to revisit the adequacy of such recommendations in this light. This topic deserves further research that is beyond the scope of this study.

For the synthetic records, we limited our analyses to the usable bandwidth specified by the developers to ensure that nonlinear response statistics were computed only within the intended range of applicability of the ground motion simulation model. Table 2 lists the usable period range of each model, as well as a summary of the type and number of records provided in each dataset that were discussed earlier. Note that all models are usable up to 4.0s with the exception of the LLNL model, which is limited to 2.0s. For the interested readers, a brief description of the methodology used by each group of seismologists to generate the synthetic time-histories is given in Appendix A. These descriptions were provided directly by the authors of each model.

⁹ The HP corner frequency was not available in three cases and the LP corner frequency in eight cases.

Station Name	Symbol	Distance (km)	HW/FW	HP (Hz)	LP (Hz)
Arleta	ARL	8.66	NU	0.12	23
Canoga Park, Topanga Canyon	CNP	14.70	HW	0.05	30
Jensen Filter Plant	JEN	5.43	HW	0.08	unknown
Simi Valley - Katherine	KAT	13.42	HW	0.5	30
LA 00	LA0	19.07	NU	0.3	unknown
LA Dam	LDM	5.92	HW	0.1	unknown
Newhall	NWH	5.92	FW	0.12	23
Pacoima Dam	PAC	7.01	FW	0.16	23
Pardee - SCE	PAR	7.46	FW	0.5	20
Pacoima Kagel Canyon	PKC	7.26	NU	0.14	23
Sun Valley - Roscoe	RO3	10.05	NU	0.1	30
Rinaldi Receiving Station	RRS	6.50	HW	unknown	unknown
Sylmar Converter Stn. East	SCE	5.19	HW	unknown	unknown
Sylmar Converter Stn.	SCS	5.35	HW	unknown	unknown
Sepulveda VA	SPV	8.44	HW	0.1	unknown
Santa Susana	SSU	16.74	HW	0.2	unknown
Northridge - Saticoy	STC	12.09	HW	0.1	30
Sylmar Hospital	SYL	5.30	FW	0.12	23
Tarzana - Cedar Hill	TAR	15.60	NU	0.1	23
Newhall - W. Pico Canyon	WPI	5.48	NU	0.05	30

Table 1: List of the twenty recording stations for the 1994 Northridge earthquake accelerograms, including the Butterworth filter corner frequencies for the recorded accelerograms. Legend: HW = hanging wall, FW = foot wall, NU = neutral, HP = high-pass corner frequency, LP = low-pass corner frequency.

Modeler	Components	# Records	Usable Bandwidth
Beresnev	Average	20	0.1s – 4.0s
Dreger	Separate	40	0.1s – 4.0s
Gusev	Separate	40	0.1s – 4.0s
LLNL	Separate	24	0.1s – 2.0s
Silva	Average	20	0.1s – 4.0s
URS	Separate	40	0.1s – 4.0s
Zeng	Separate	40	0.1s – 4.0s
Real	Separate	40	0.1s – 4.0s

Table 2: Summary of synthetic ground motion datasets.

3.0 Description of the SDOF Structures

The eight datasets of records described in the previous section were applied to 46 5%-damped nonlinear Single-Degree-of-Freedom (SDOF) oscillators with natural periods ranging from 0.1 to 4.0s. The backbone force-deformation curve was bilinear with 2% post-yield hardening and a hysteretic rule that had no degradation of either strength or stiffness. The selected period range, which encompasses the fundamental periods of typical engineering structures, is, with the exception of the LLNL dataset, within the usable bandwidth of each ground motion model (see Table 2).

To ensure a response that ranged from mildly inelastic to severely inelastic, we selected five “strength” levels for the SDOF system at each oscillator period. In addition, we also included in this study the elastic response case both for completeness and for checking purposes. The nominal strength levels of the SDOF oscillators were set as a fraction of peak elastic base shear, which follows the common seismic design practice of reducing the structural strength for a ductile structure by a force reduction factor, R . The five selected strength levels are characterized by R values equal to two (mildly inelastic), four, six, eight, and ten (severely inelastic). Note that the level of nonlinear responses imply, for some SDOF systems, very large ductility values that, of course, may not be physically attainable by all real structures.

The peak value of the elastic base shear, or equivalently the peak elastic deformation, experienced by an elastic structure is, however, a ground-motion-specific quantity. Therefore, one can achieve the same value of R either a) for *each record* in a dataset or b) on an *average sense for all the records* in the same dataset.

In the former case the same target R value can be achieved by varying the yield displacement of the structure, d_y , from record to record. More precisely, for each record d_y needs to be set equal to the peak elastic displacement for that record divided by the desired value of R (see Figure 1). This case is hereinafter referred to as “constant- R ” case. In this set of analyses each record is effectively applied to SDOF systems with slightly different strength characteristics.

In the latter case, the same R value can be obtained in multiple ways. In this study we kept constant the yield strength, F_y , of the oscillator for all the records and we set its value equal to the *median* peak elastic response displacement across all the records in the real dataset divided by R . This is, of course, equivalent to keeping the yield strength, F_y , constant. In this way the same structure, with an “average” strength, that varies with any given period and R -value, is used to evaluate the nonlinear response to all the records. This case is hereinafter referred to as “constant-strength” (or constant- F_y) case.

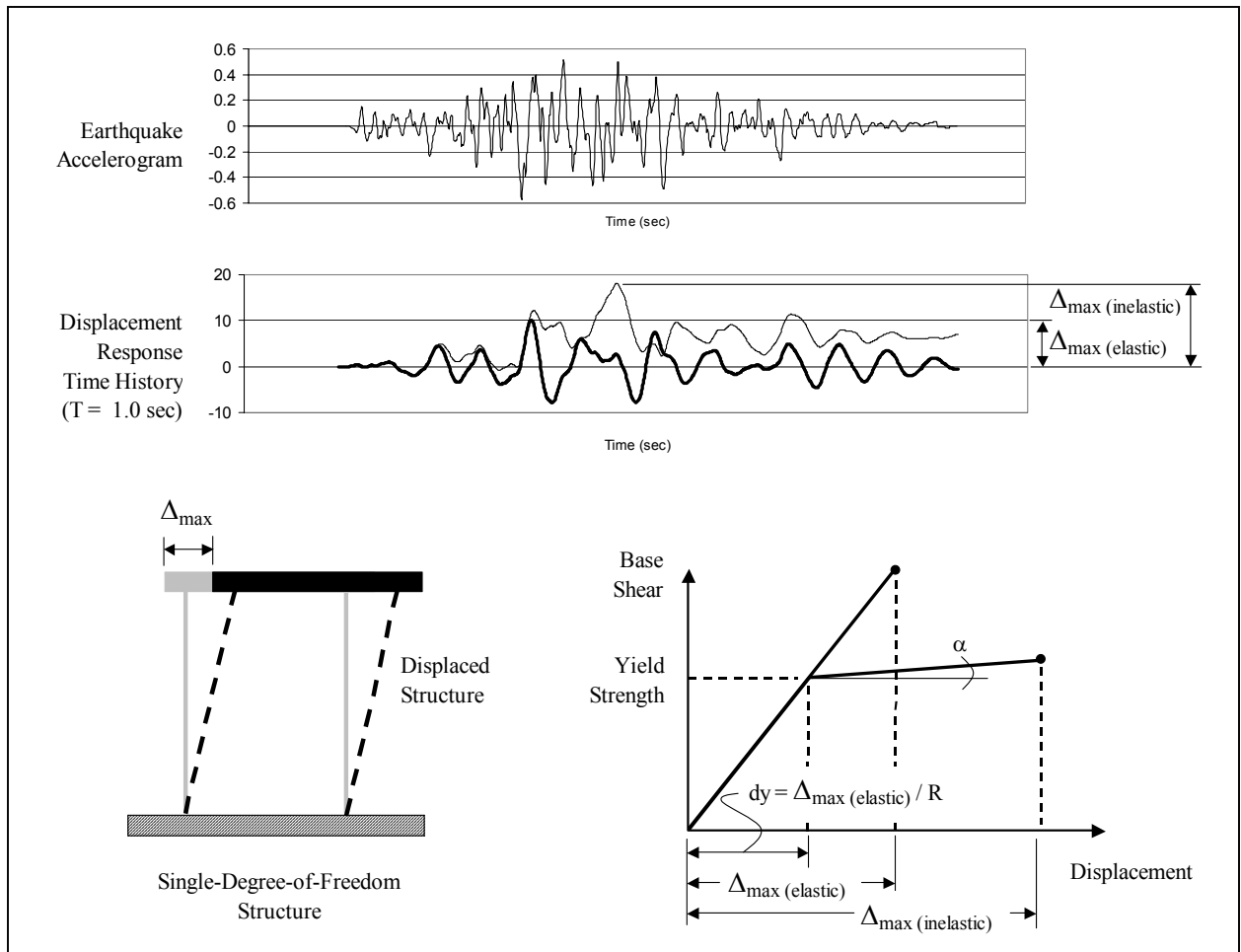


Figure 1: Schematic of SDOF structure and yield strength definition. The quantity α is the post-yield hardening here set equal to 2%. The yield strength in the figure is called F_y in this study.

In this study, we considered both constant-R and constant-strength analyses. The constant-strength case was selected as the primary focus of our investigations because of its simpler physical interpretation. For conciseness, we often neglected to remind the reader that the results were obtained using the constant-strength alternative. The results found using the alternative constant-R approach are, however, clearly marked. Nonlinear response spectra from both sets of analyses are briefly compared and contrasted in Section 4.4.

4.0 Results

The comparison of SDOF responses generated using different datasets is conveniently accomplished using the median (calculated as the geometric mean) and a standard deviation (of the natural logarithms of the data) of the 5%-damped elastic and inelastic spectra computed for the 20 stations (12 for the LLNL case). The spectra for each station are calculated for the “average” horizontal component in the sense explained in Section 2. It is legitimate to use statistics across all the stations in this context because they are all within 20 kilometers from the fault rupture (Table 1), which is a fairly tight distance range.

Figure 2 shows the median *elastic* pseudo-acceleration spectrum (panel *a*) and corresponding standard deviations (panel *b*) across stations in log-log scale for each synthetic dataset as well as for the real record one. Figure 3 displays the same results plotted as the ratio of the same quantities, that is the median in the top panel and the standard deviation in the bottom panel, for each synthetic model to the corresponding ones for the real dataset. A ratio above unity, if statistically significant, means overestimation of the response by a model and below unity means underestimation¹⁰.

From inspecting the graphs in the top panels of Figures 2 and 3, it is clear that the median spectral amplitudes and shapes of the response spectra for some of the seven simulated cases is quite different than the median response spectrum from the real recordings. This amplitude difference can be large, especially in the short period range (up to about 80% at 0.1s). It is also interesting to note that only the model developed by Gusev provides a median elastic spectrum that is within $\pm 20\%$ of the median spectrum from the real Northridge records across the entire frequency range. The LLNL model also is within $\pm 20\%$ of the target for almost all its range of applicability, which has an upper bound of 2s. All the other models tend to overestimate by different amounts the elastic response of SDOF systems with periods below 0.3s and, with the exception of the models by URS and Zeng, to underestimate it above 0.3s. The URS and Zeng models seem to provide elastic responses even at periods larger than 0.3s that are, always in an average sense, either equally or more severe than those of the real records. Finally, any trend across period in the median ratios shown in Figure 3 that departs from a horizontal line suggests that the elastic spectra generated by the synthetic model have, on average, a different shape than those produce by nature, at least in this Northridge earthquake test case.

¹⁰ In Figure 1 we have used pseudo-acceleration to produce the elastic spectra because most of the engineers are accustomed to seeing spectra in acceleration terms rather than in displacement terms. All the figures that follow, however, use displacement response spectra because displacement is the quantity most widely use when dealing with post-elastic response of structures.

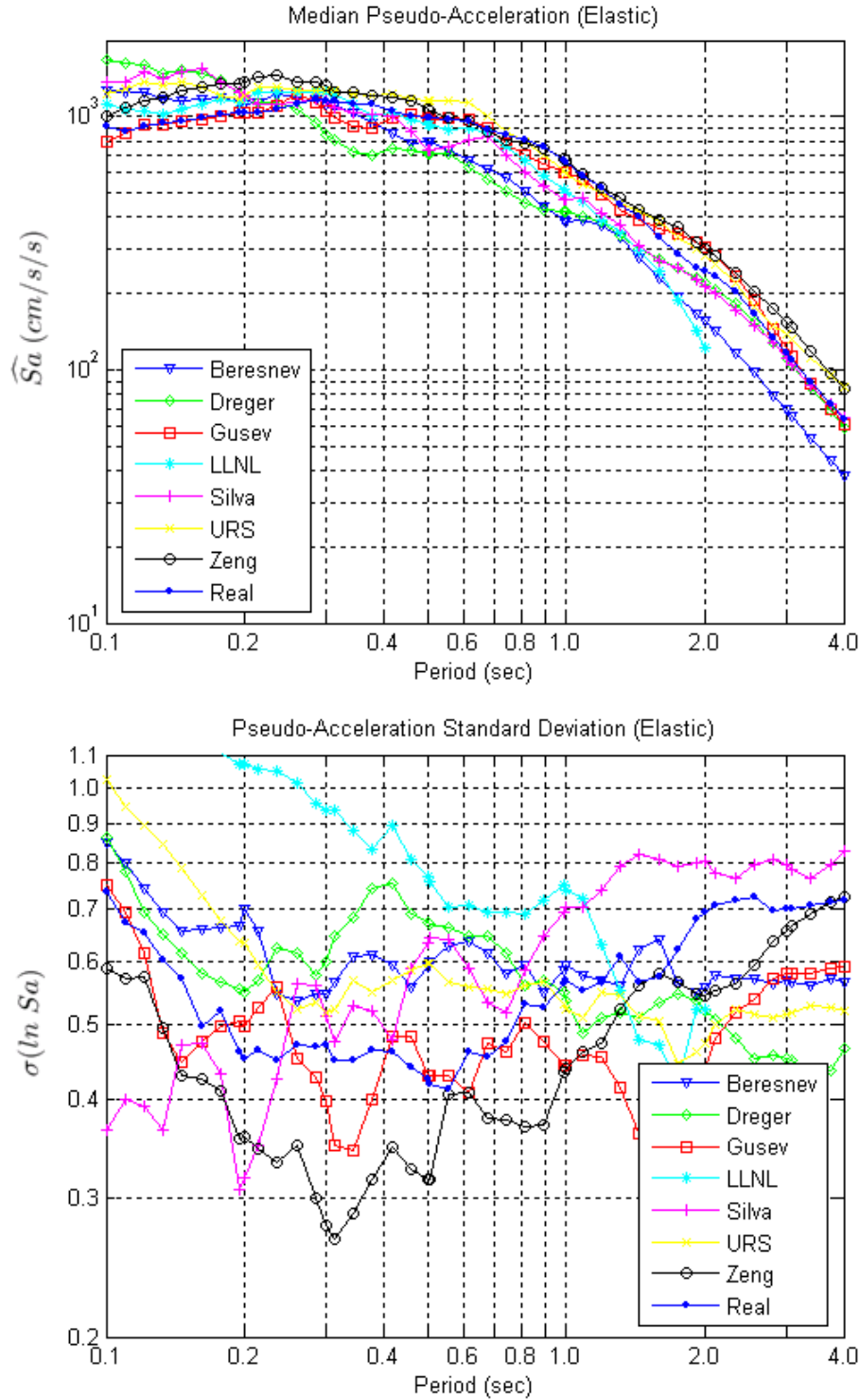


Figure 2: Median (top panel) and standard deviation (bottom panel) of the 5%-damped *elastic* pseudo-acceleration response spectra for the “average” horizontal component computed for all the available stations (12 for the LLNL model and 20 in the other seven cases). Note: 981 cm/s/s is equal to one g .

Note that the dispersion in the record-to-record ratio of inelastic spectra (not shown here) decreases with increasing period. The values of the COV vary with the model and they range between 0.3 at 4s to more than 1.0 at 0.1s. Hence, given these COV values and a sample size of 20 records per model (12 for the LLNL one), we can state that the elastic spectral ratios in Figure 3a are different than one with 90% confidence either in the long period range, or in the short period range, or in both for all seven models but Gusev's. More precisely, the period ranges where the ratios significantly differ from one are approximately above 0.6s for Beresnev, above 0.3s and below 0.15s for Dreger, above 1.5s for LLNL, between 0.8s and 1.1s and below 0.15s for Silva, above 3s and below 0.15s for URS, and above 1.5s for Zeng.

The inspection of the bottom panel of Figures 2 and 3 shows that none of the synthetic models provide a dispersion measure of the linear responses that is within $\pm 20\%$ of those from the real ones across the entire frequency range. The standard deviation across frequency from all the models, with the exception of the LLNL one for periods below 0.8s, is within $\pm 40\%$ with only minor departures from it. The LLNL model, on the other hand, seems in this case to provide records that produce significantly more variable elastic responses in the short period range than those from nature. Recall, however, that the statistics for the LLNL model are based on 12 records only and not 20 like in the other cases.

We presented here a short summary of the elastic results, which were more thoroughly investigated in the PEER K201 Treasure Island project, only to set the stage for the post-elastic nonlinear results that are the core of this study. The differences in the elastic response between the simulated and real records have an influence on the nonlinear response statistics at all strength levels. This is apparent from Figure 4, which presents the ratio of the medians and standard deviations of the inelastic *displacement* response spectra for the R=2 case. Note that for all the figures that relate to nonlinear post-elastic responses we measure the response in terms of spectral displacement rather than pseudo-spectral acceleration as we did in the linear elastic case. The spectral ratios displayed in Figure 3, of course, are not affected by which one of these two variables is used for the spectra. The signature of the elastic results in Figure 3 is obvious in the post-elastic ratios displayed in Figure 4. The trend of the ratios for R=1 and R=2 for each modeler are very similar. A similar statement, although less strong due to the increase in the record-to-record response variability for larger values of R, can be made for the more severely nonlinear cases.

A convenient way of investigating the effects of each modeling technique *above and beyond the elastic regime* is to normalize the nonlinear displacement response spectra generated for a given value of R (greater than one) by the corresponding elastic spectra obtained using the same dataset of synthetic records. We will refer to this ratio of inelastic-to-elastic spectra as C , that is:

$$C = \frac{(S_d)_{\text{nonlinear}}}{(S_d)_{\text{elastic}}} \quad (1)$$

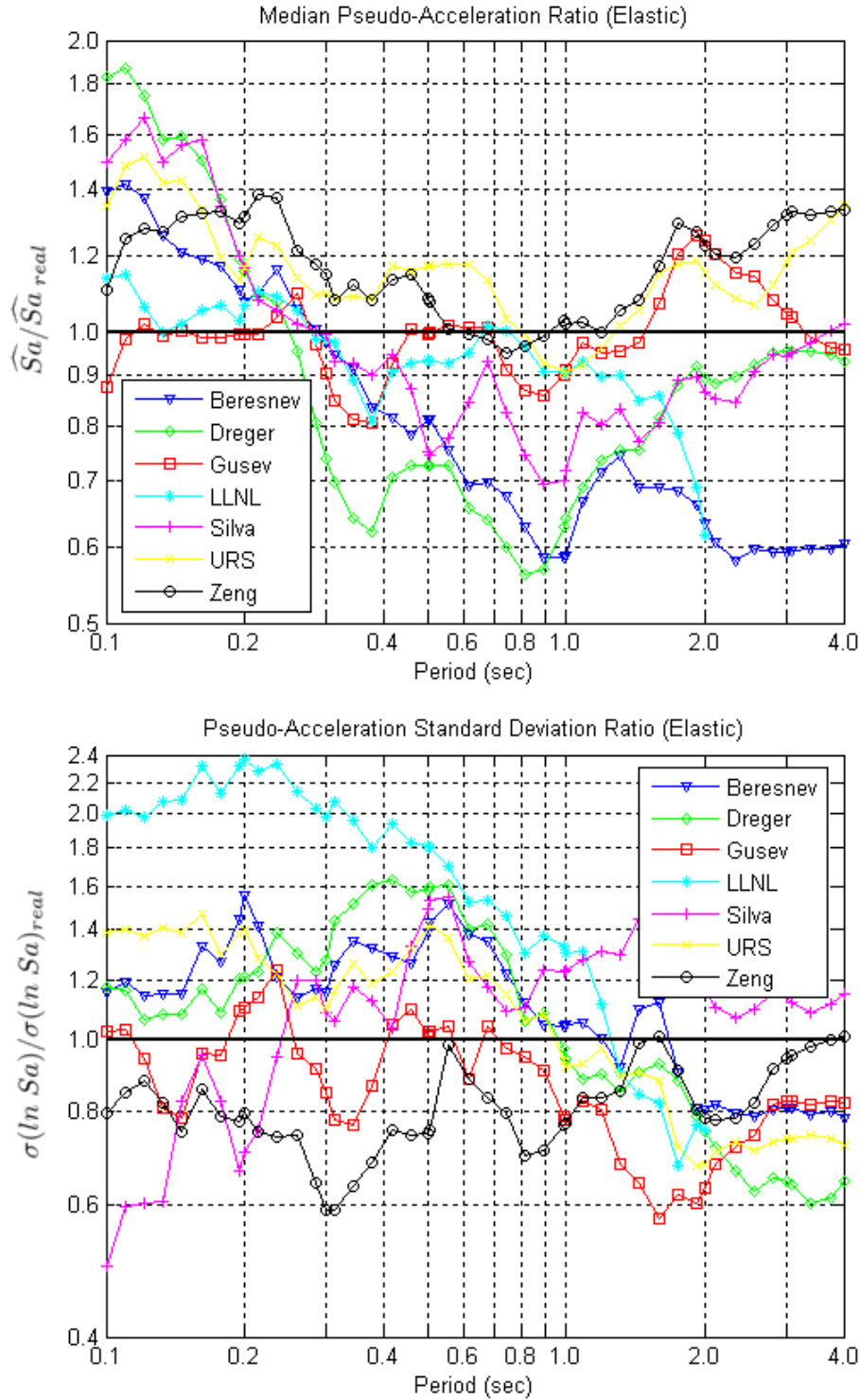


Figure 3: Ratio of the medians (top panel) and standard deviations (bottom panel) of the 5%-damped linear *elastic* displacement response spectra of each synthetic model to the corresponding quantity computed for the real record dataset.

Of course, C is a function of the oscillator period, T . In addition, given that we are comparing the results from synthetic datasets with the target ones from the real recordings, it is useful to divide the quantity C by the inelastic-to-elastic spectra ratio obtained for the real records, C_{real} . The quantity C (or C_{real} in the case of real records) is the response measure for which median values and standard deviations across the twenty recording stations (or twelve in the LLNL case) are computed. Also, for conciseness of notation, the ratio of C/C_{real} is sometime called q_c in the sections that follow. Namely:

$$q_c = \frac{C}{C_{real}}, \quad (2)$$

The value of C is, on average, greater than one only for short periods (the shorter the period, the larger the average value of C), whereas it tends to one for moderate to longer periods (e.g., greater or equal to 1.0s). This is essentially the well-known equal displacement rule that was introduced by Veletsos and Newmark (1960) some forty years ago. The quantity C can be interpreted as a correction to the linear maximum elastic displacement to obtain the maximum nonlinear displacement of an SDOF oscillator.

In the following sections we will present the differences (as ratios) in C between synthetic and real ground motions. We will also briefly discuss the influence of the component averaging method and the impact of the yield strength definition on the observed results. Finally, we will report some results that were obtained by replacing the spectral displacement as the nonlinear structural response measure with energy-based quantities, such as the input energy and the absorbed energy.

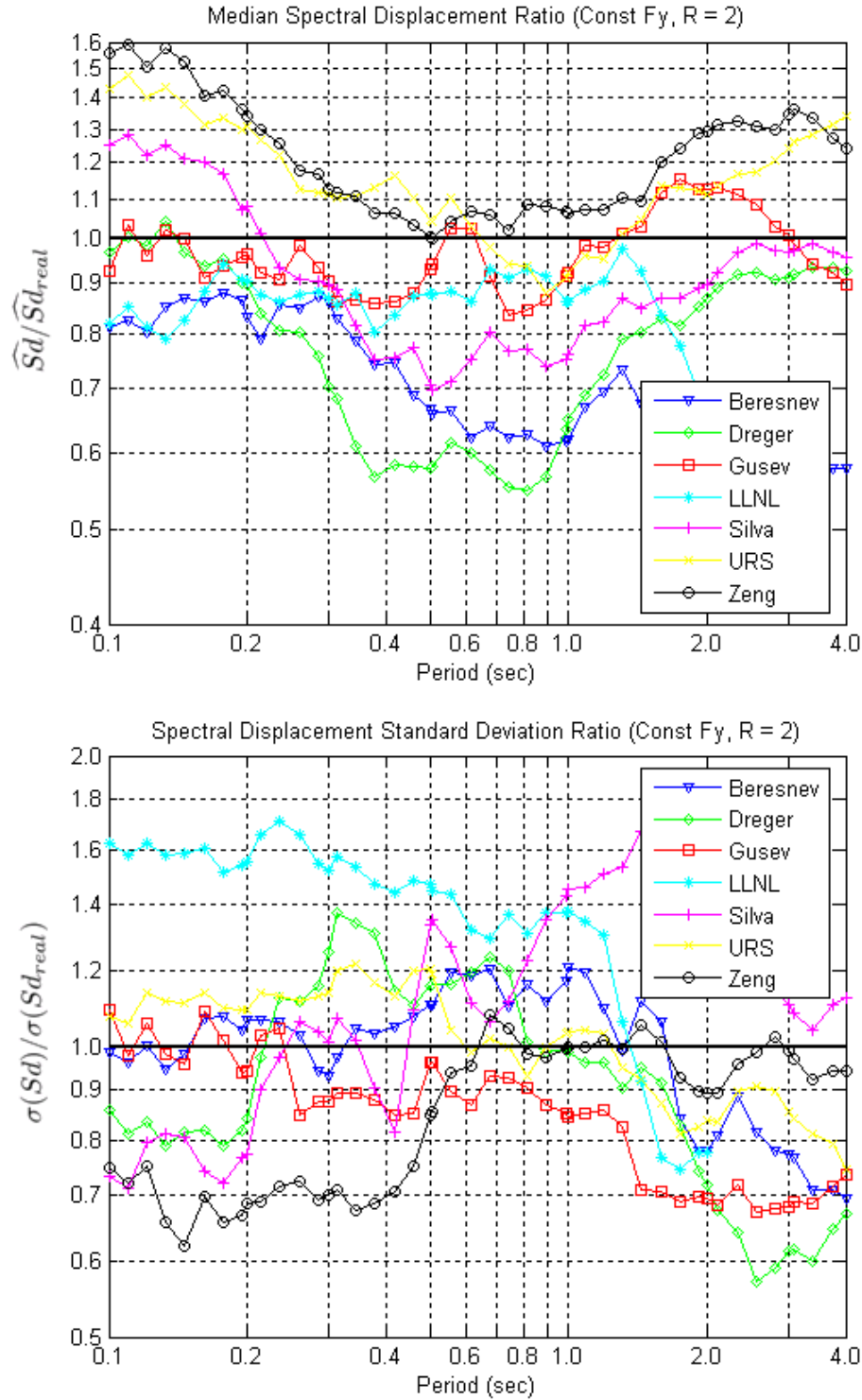


Figure 4: Ratio of the medians (top panel) and standard deviations (bottom panel) of the 5%-damped *nonlinear* response spectra (R=2) of each synthetic model to the corresponding quantity computed for the real record dataset.

4.1 Nonlinear Structural Response to Simulated and Real Ground Motions

The median value¹¹, \hat{C} , of the inelastic-to-elastic spectral ratio C for each of the seven synthetic datasets divided by the median value, \hat{C}_{real} , of C for the real records is plotted across the period range of 0.1s to 4.0s in panel (a) of Figures 5 to 7. The bottom panel shows the ratio of the standard deviation of C divided by the standard deviation of C_{real} . Attention is focused on the C/C_{real} results for strength levels $R = 2, 4$ and 10 . The results for strength levels $R = 6$ and 8 are similar to those for $R=10$ and, therefore, they are not shown here.

4.1.2 Median responses

A deviation above unity of any of the \hat{C}/\hat{C}_{real} curves in the top panel of Figures 5 to 7 indicates that, median *elastic response* for a simulated and the real record datasets *being equal*, the synthetic records in that dataset tend to produce, on average, systematically larger nonlinear spectral displacements than those by real records. Conversely, deviations below unity indicate that the simulated records tend to be, on average, more benign in producing nonlinear responses than those in nature. It is emphasized here that the equality of the linear responses generated by simulated and real records is postulated here only as a tool to compare the effectiveness of synthetic and real records in creating *nonlinear* responses. From Figure 3a, however, it is clear that this equality is often not statistically achieved for some of the seven simulated datasets at some period ranges. In the rest of this section we will assume that this equality of linear responses holds.

From the top panel of Figures 5 to 7 it is apparent that the difference in the ratio of median nonlinear to elastic response between the synthetic datasets and the real records is more period-dependent for some ground motion models than for others. For example, the \hat{C}/\hat{C}_{real} results for $R=2$ in Figure 5a show that all the models provide nonlinear responses that are within $\pm 20\%$ from those of the real ones for all periods larger than about 0.3s. For periods shorter than 0.3s the records generated by the models by Beresnev, Dreger, LLNL, and, at some periods, Silva tend to be significantly less aggressive than real records. Conversely, the model by Zeng seems to create records that are, on average, more damaging. As before, the model by Gusev, being always within $\pm 10\%$ of the target, appears to be the more accurate one overall. For $R=4$ and $R=10$ in Figures 6 and 7, the models by Gusev, URS, and Zeng produce nonlinear responses that are statistically closest to those created by real records. The other four models provide similarly accurate results only for long periods, while in the region of shorter periods they seem to generate significantly less severe responses than their real counterparts. These systematically benign responses are more prominent at shorter periods for a given R , and in general at all periods for larger R values. A summary of the peak and average values of \hat{C}/\hat{C}_{real} across the period range is given in Table 3, along with the structural periods at which the peak values occur.

¹¹ The median value was computed as the geometric mean, i.e., the exponential of the mean of the natural log of the ratios across all the available stations (i.e., 12 for the LLNL case and 20 for all other cases).

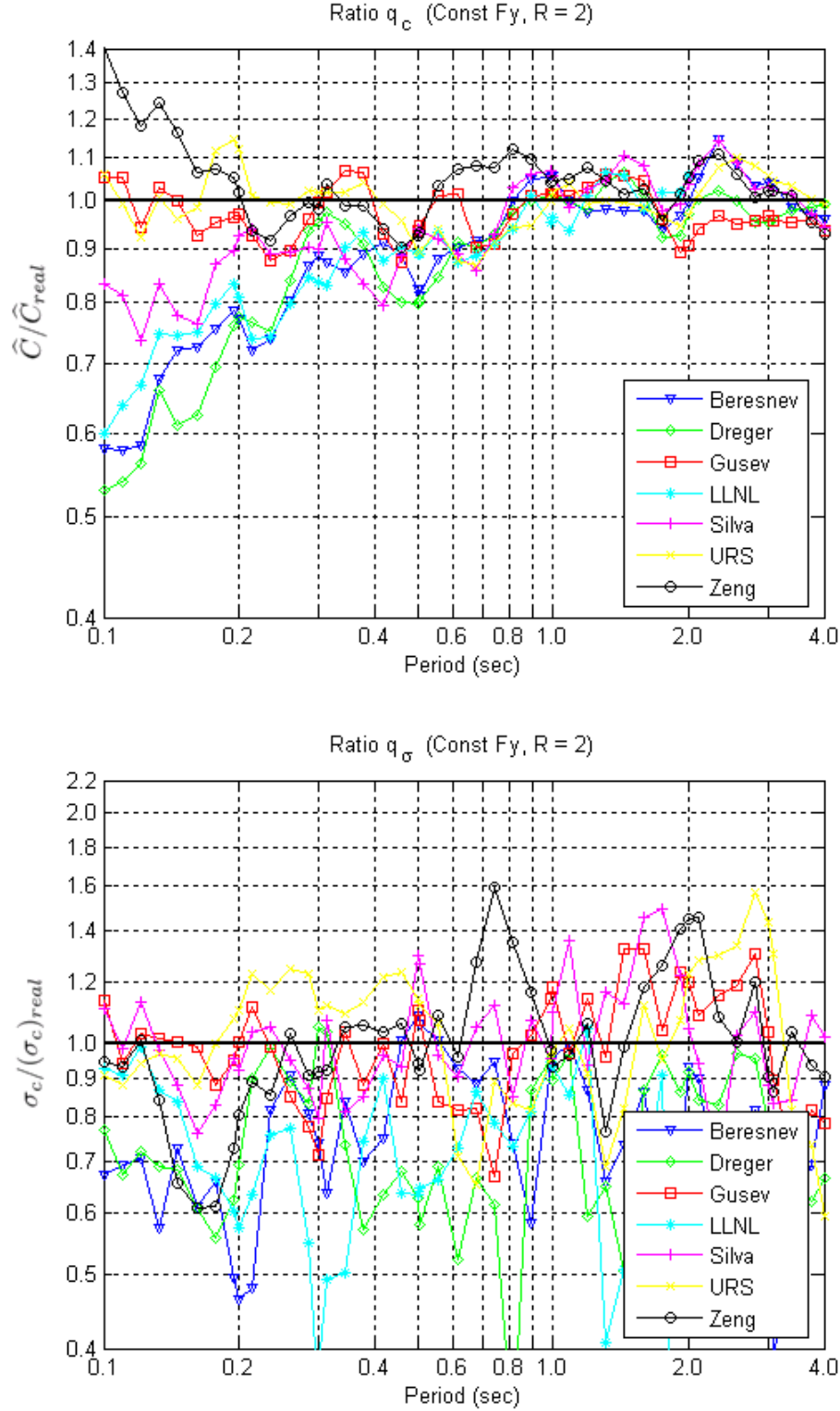


Figure 5: Statistics of the inelastic-to-elastic spectral ratio, C , for the seven synthetic datasets, normalized by the corresponding quantity, C_{real} , obtained from the suite of real records, for a level of inelasticity defined by $R=2$. The top panel presents the ratio of the medians while the bottom panel displays the ratio of the standard deviations.

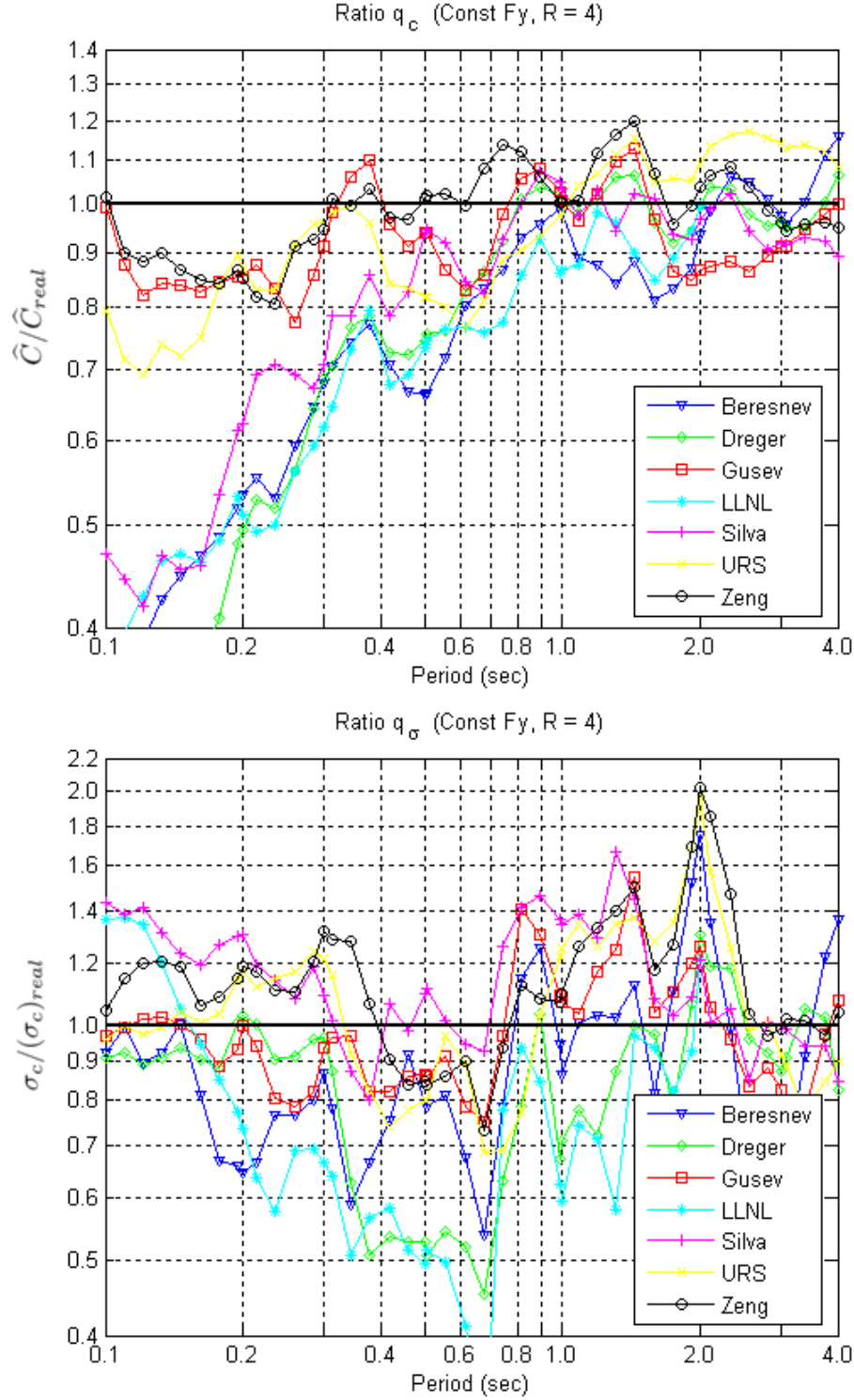


Figure 6: Statistics of the inelastic-to-elastic spectral ratio, C , for the seven synthetic datasets, normalized by the corresponding quantity, C_{real} , obtained from the suite of real records, for a level of inelasticity defined by $R=4$. The top panel presents the ratio of the medians while the bottom panel displays the ratio of the standard deviations.

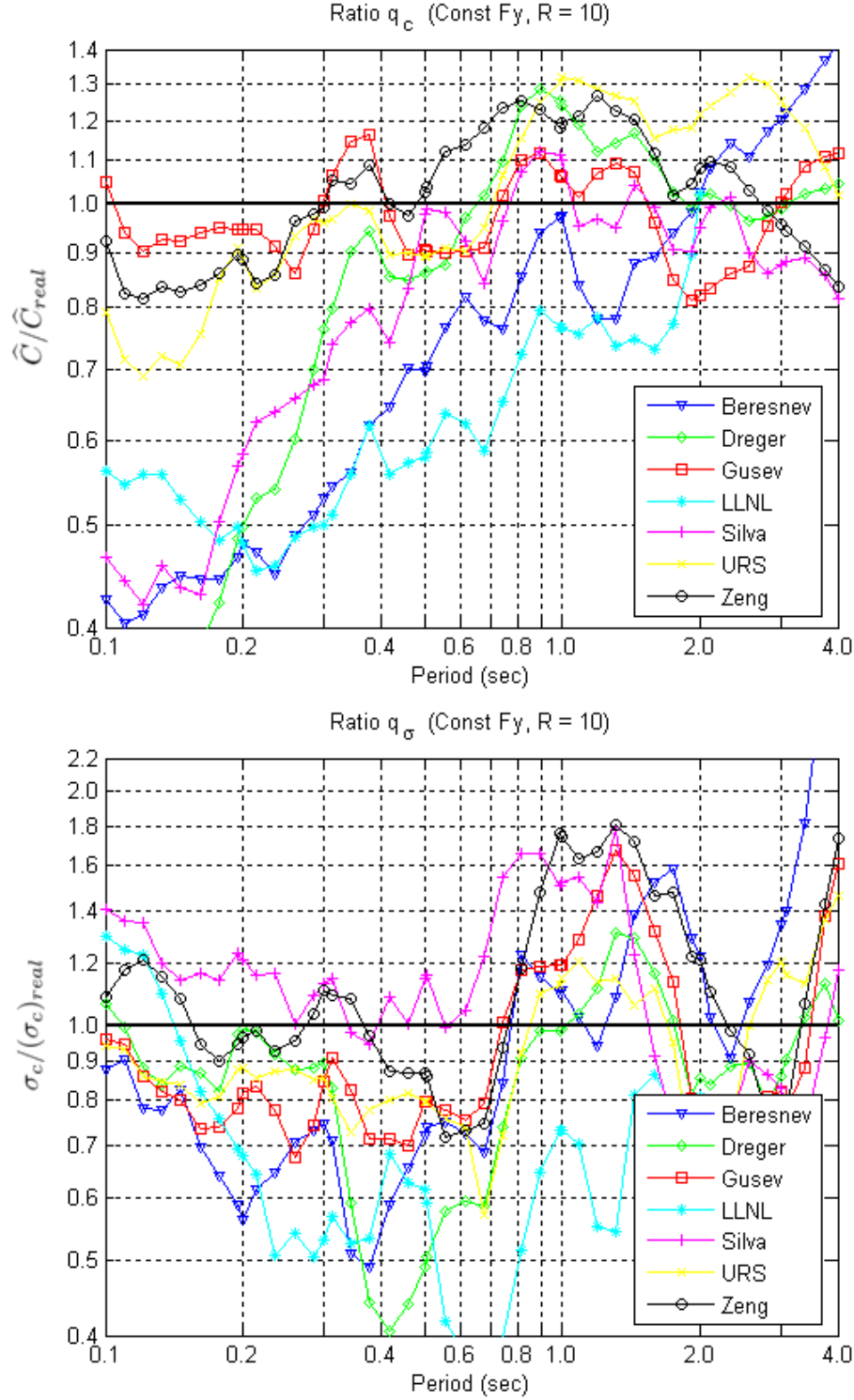


Figure 7: Statistics of the inelastic-to-elastic spectral ratio, C , for the seven synthetic datasets, normalized by the corresponding quantity, C_{real} , obtained from the suite of real records, for a level of inelasticity defined by $R=10$. The top panel presents the ratio of the medians while the bottom panel displays the ratio of the standard deviations.

Model	R = 2					R = 4					R = 10				
	Min	T _{min}	Max	T _{max}	Avg	Min	T _{min}	Max	T _{max}	Avg	Min	T _{min}	Max	T _{max}	Avg
Beresnev	0.58	0.11	1.15	2.32	0.90	0.38	0.11	1.16	4.00	0.77	0.40	0.11	1.41	4.00	0.78
Dreger	0.53	0.10	1.06	1.44	0.88	0.30	0.11	1.07	1.44	0.78	0.32	0.11	1.28	0.90	0.86
Gusev	0.88	0.46	1.07	0.35	0.97	0.78	0.26	1.13	1.44	0.93	0.81	1.92	1.17	0.38	0.98
LLNL	0.60	0.10	1.07	1.31	0.88	0.39	0.11	1.00	2.00	0.70	0.45	0.21	1.02	2.00	0.62
Silva	0.74	0.12	1.14	2.32	0.95	0.42	0.12	1.07	0.90	0.82	0.42	0.12	1.12	0.90	0.81
URS	0.87	0.67	1.15	0.19	1.00	0.69	0.12	1.17	2.55	0.95	0.69	0.12	1.32	2.55	1.04
Zeng	0.90	0.46	1.41	0.10	1.04	0.81	0.24	1.20	1.44	0.99	0.81	0.12	1.26	1.19	1.02

Table 3: Peak and average values of \hat{C}/\hat{C}_{real} for strength levels R = 2, 4 and 10. The table shows also the structural periods at which each peak value of \hat{C}/\hat{C}_{real} occurred.

To determine the statistical significance of the observed $q_c = \hat{C}/\hat{C}_{real}$, the 2-sided 90% t-student confidence limits for q_c were calculated across the period range at each strength level for each ground motion model. At oscillator periods where the upper and lower confidence limits do not bracket the line $\hat{C}/\hat{C}_{real} = 1$, the median nonlinear spectral displacement for the synthetic dataset is statistically biased at a 10% level of significance. Figures 8 to 14 show the confidence limits for each ground motion model at the three key structural strength levels. As anticipated, only the model by Gusev seems to be unbiased across the whole spectrum of periods regardless of the level of nonlinearity. In general, with the exception of the two by Beresnev and Dreger, all the models are unbiased for R=2 across the entire period range. All the models but Gusev's are biased at some periods for R=4 and R=10. The amount of bias is larger for larger R values and for shorter periods. In these cases most of the synthetic models create records that are more benign than real ones. The model by URS, on the other hand, is the only one that creates records that produce statistically more severe inelastic responses at the R=10 level than those in nature for SDOF oscillators of 0.8s and longer natural period.

The average deficiency of the *nonlinear* responses generated by some of these synthetic ground motions at short periods (e.g., below 0.3s) is likely due to a systematic difference in that period range in the average shape of the *linear* response spectra generated by synthetic and by real records. Figure 2a shows, in fact, that some of the models, such as Beresnev and Dreger, on average, produce linear pseudo-acceleration spectra that are either flat or falling instead of climbing with increasing periods below 0.3s like the spectrum from real records does. The difference in spectral shape is more evident in Figure 3a, which shows the ratio of the elastic spectra for the synthetic models and the real ones. Given this discrepancy, it is not surprising that when the effective period of the oscillator lengthens because of the nonlinear behavior of the oscillator these records become less aggressive than real ones.

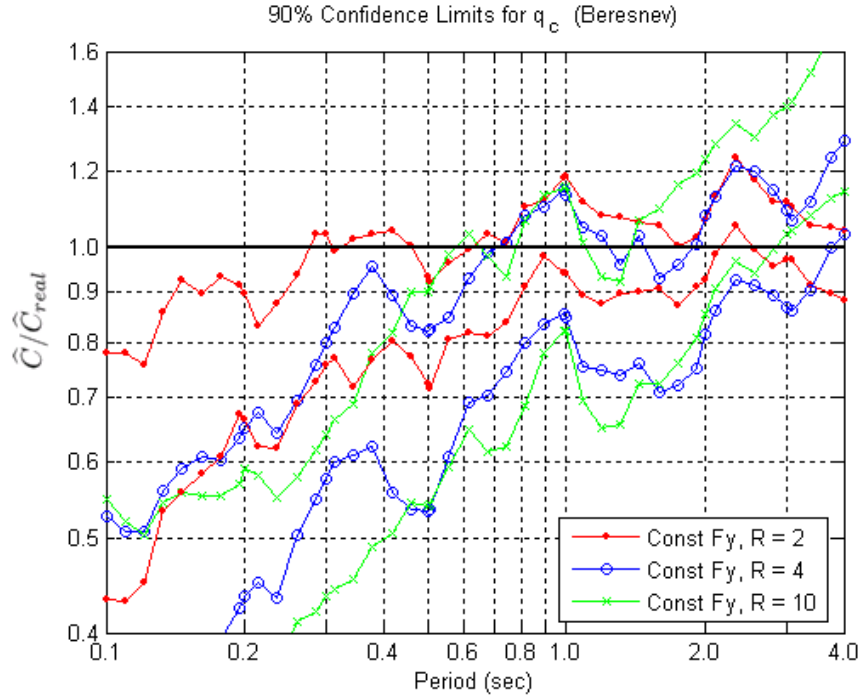


Figure 8: Upper and lower 90% confidence limits for q_c for constant-strength levels $R = 2, 4$ and 10 for the Beresnev model. The ratio is significantly different than one at those periods where the unity line is not bracketed by the lower and upper bounds of the confidence band.

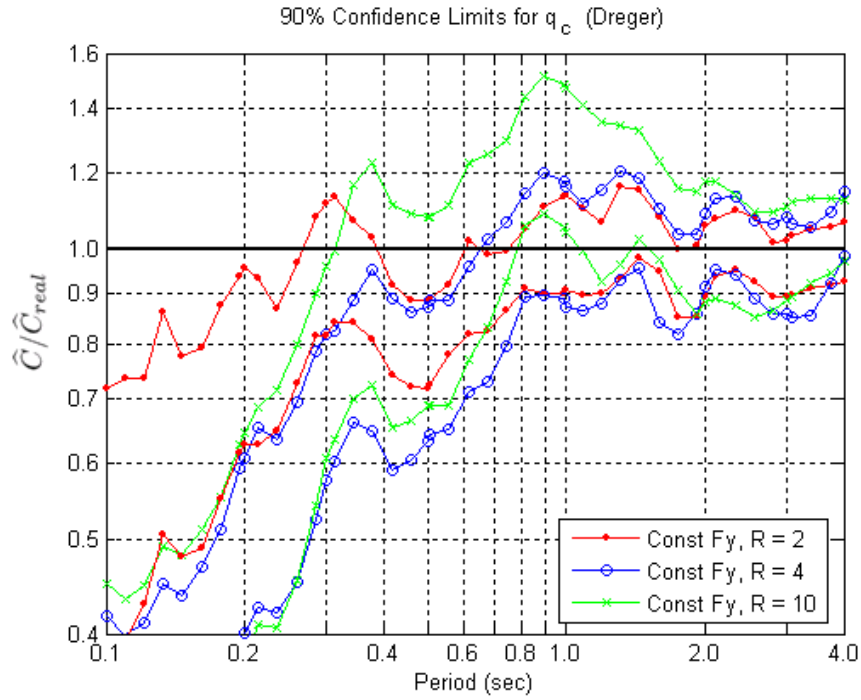


Figure 9: Upper and lower 90% confidence limits for q_c for constant-strength levels $R = 2, 4$ and 10 for the Dreger model. The ratio is significantly different than one at those periods where the unity line is not bracketed by the lower and upper bounds of the confidence band.

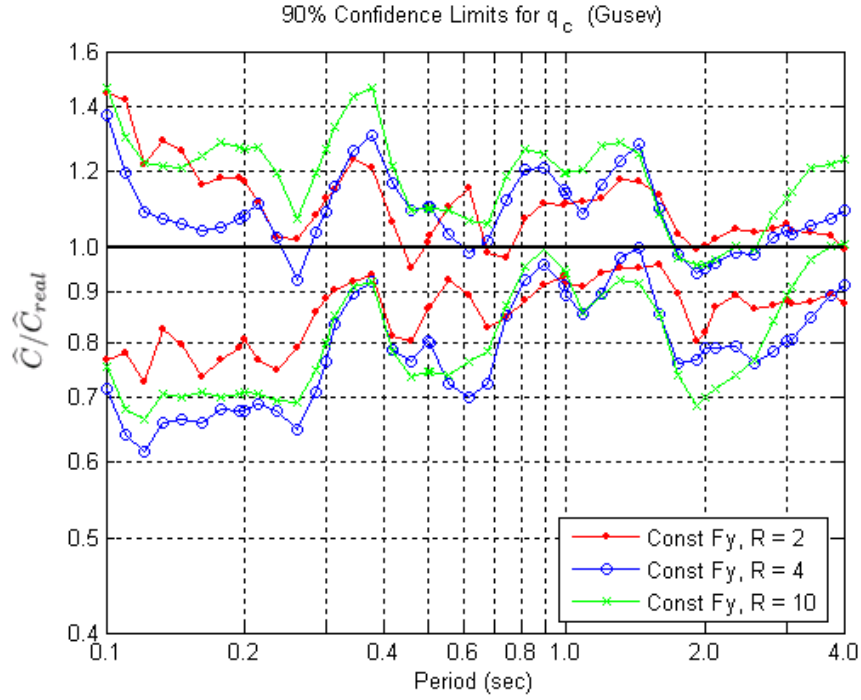


Figure 10: Upper and lower 90% confidence limits for q_c for constant-strength levels $R = 2, 4$ and 10 for the Gusev model. The ratio is significantly different than one at those periods where the unity line is not bracketed by the lower and upper bounds of the confidence band.

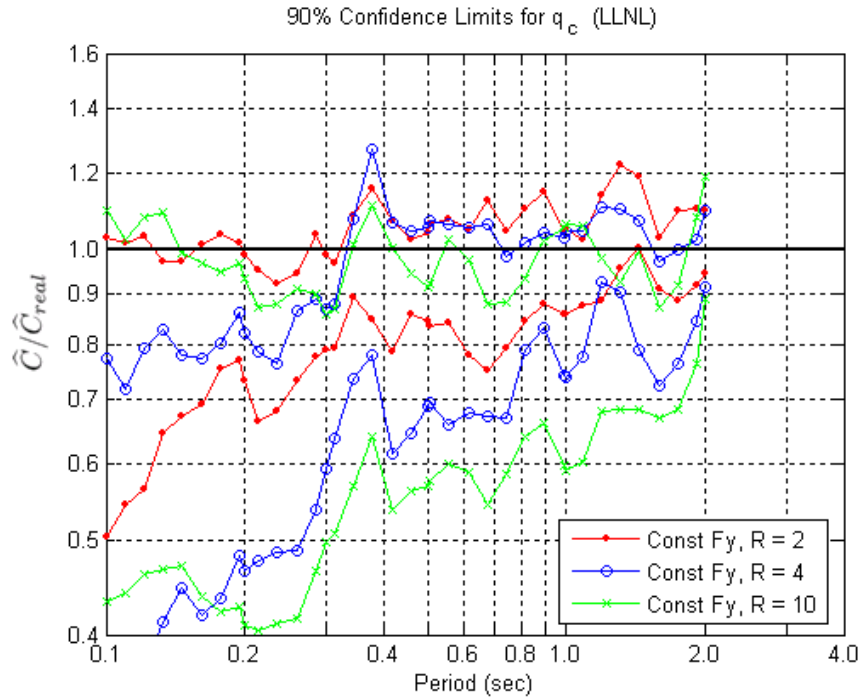


Figure 11: Upper and lower 90% confidence limits for q_c for constant-strength levels $R = 2, 4$ and 10 for the LLNL model. The ratio is significantly different than one at those periods where the unity line is not bracketed by the lower and upper bounds of the confidence band.

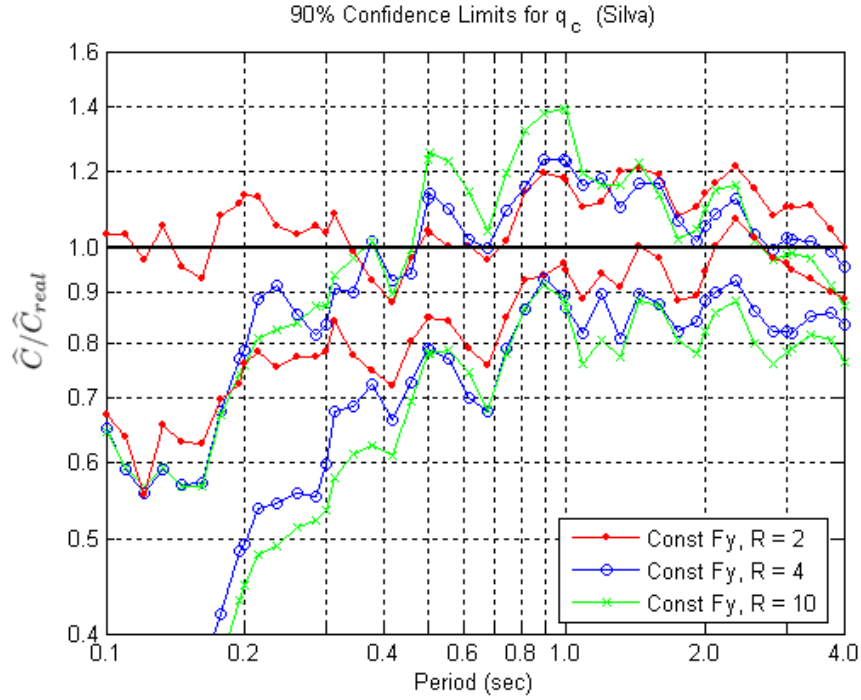


Figure 12: Upper and lower 90% confidence limits for q_c for constant-strength levels $R = 2, 4$ and 10 for the Silva model. The ratio is significantly different than one at those periods where the unity line is not bracketed by the lower and upper bounds of the confidence band.

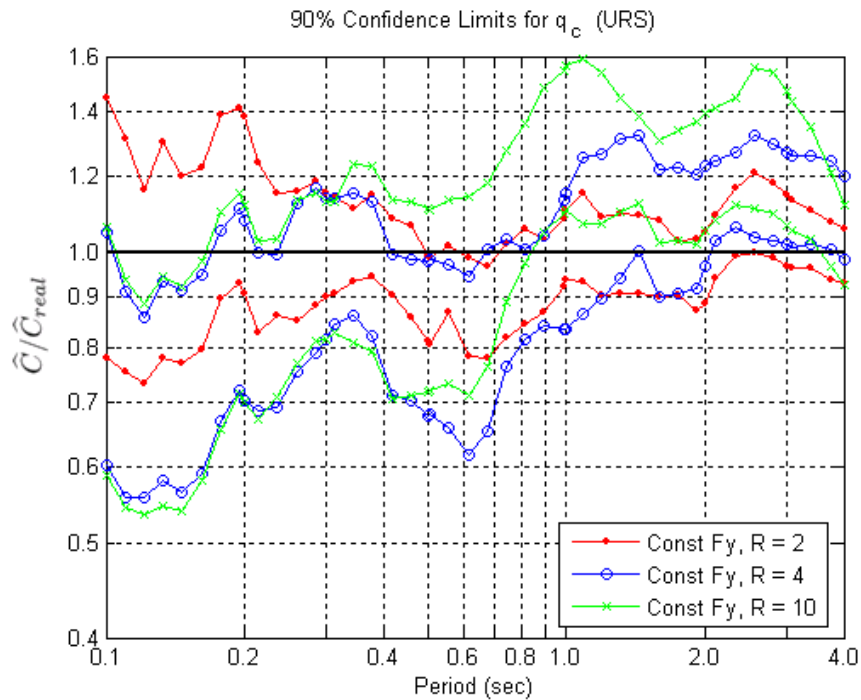


Figure 13: Upper and lower 90% confidence limits for q_c for constant-strength levels $R = 2, 4$ and 10 for the URS model. The ratio is significantly different than one at those periods where the unity line is not bracketed by the lower and upper bounds of the confidence band.

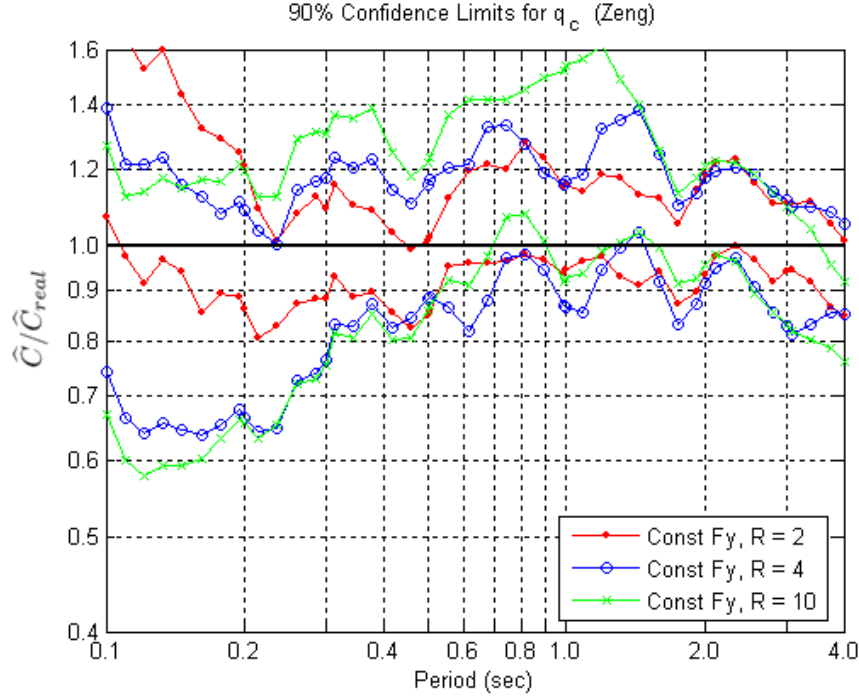


Figure 14: Upper and lower 90% confidence limits for q_c for constant-strength levels $R = 2, 4$ and 10 for the Zeng model. The ratio is significantly different than one at those periods where the unity line is not bracketed by the lower and upper bounds of the confidence band.

4.1.2 Record-to-record nonlinear response variability

The bottom panel of Figures 5 to 7 shows the relative dispersion of *nonlinear (still normalized by elastic) responses* to synthetic records and to real records. As before, a line above unity means relatively more record-to-record variability produced by synthetic records whereas the opposite is true for a line below unity. The relative variability of nonlinear responses to synthetic and real records is, again, model-dependent and varies with the level of response severity. For $R=2$ most of the models, especially those from Beresnev, Dreger, and LLNL, seem to underestimate the record-to-record variability of the response from real records, in particular at shorter periods. For the more severe responses ($R=4$ and $R=10$) the general tendency of most of the models is to underestimate the response variability for periods ranging between $0.3s$ and $0.8s$ and to overestimate it between $0.8s$ and about $3s$. A summary of statistics of $\sigma_c/(\sigma_c)_{real}$ across the period range is given in Table 4.

	R = 2					R = 4					R = 10				
Model	Min	T _{min}	Max	T _{max}	Avg	Min	T _{min}	Max	T _{max}	Avg	Min	T _{min}	Max	T _{max}	Avg
Beresnev	0.38	3.09	1.09	0.50	0.76	0.54	0.67	1.76	2.00	0.90	0.49	0.38	3.71	4.00	1.04
Dreger	0.31	0.81	1.05	0.30	0.75	0.45	0.67	1.31	2.00	0.85	0.40	0.42	1.32	1.31	0.87
Gusev	0.67	0.74	1.33	1.44	1.00	0.75	0.67	1.55	1.44	0.98	0.64	2.11	1.68	1.31	0.94
LLNL	0.07	1.92	1.04	1.19	0.69	0.28	0.67	1.37	0.11	0.77	0.31	0.67	1.30	0.10	0.69
Silva	0.69	2.32	1.50	1.74	1.02	0.80	0.38	1.67	1.31	1.15	0.69	2.11	1.78	1.31	1.14
URS	0.59	4.00	1.58	2.81	1.04	0.69	0.67	1.95	2.00	1.08	0.57	0.67	1.46	4.00	0.93
Zeng	0.61	0.16	1.59	0.74	1.01	0.73	0.67	2.01	2.00	1.15	0.72	0.56	1.81	1.31	1.13

Table 4: Peak and average values of $\sigma_c/(\sigma_c)_{real}$, which is the ratio of the standard deviation of C for simulated records to the standard deviation of C_{real} . The values are reported for strength levels $R = 2, 4$ and 10 . Included are also the SDOF periods at which each peak value of $\sigma_c/(\sigma_c)_{real}$ occurred.

If synthetic records tend to generate less variable nonlinear responses than real ones, then simple statistical considerations show that an analyst would be better off using them rather than real ones to estimate the *median* nonlinear response of a structure¹² for a given earthquake scenario. From a practical standpoint, the same accuracy would be achieved with fewer runs with simulated rather than real records as input. However, if an engineer seeks to design a new structure or assess the safety of an existing one against collapse, for example, the use of simulated records that tend to generate less variable responses would underestimate the likelihood of extreme response values and, therefore, the chances of collapse. This shortcoming should be taken into consideration.

¹² This statement assumes that the synthetic ground motions generate statistically unbiased responses. If that is untrue, like in a few cases among those considered here, the bias needs to be corrected when using such records.

4.2 Influence of Response Component Averaging Method

To determine if using the geometric mean of the response to both horizontal components at each station rather than the root-mean-square, as done so far, would result in different trends in the results, we investigated the following ratio:

$$q_{avg} = \frac{\hat{C}_{RMS}}{\hat{C}_{geometric}} \quad (3)$$

where \hat{C}_{RMS} and $\hat{C}_{geometric}$ are the median values of the inelastic-to-elastic spectral ratio C across the available stations computed using the two different averaging schemes. The averaging method is pertinent to only five of the seven simulation models: Dreger, Gusev, LLNL, URS, and Zeng. Beresnev and Silva provided only one “average” ground motion component per station and, therefore, the results for their models will not be affected by the averaging technique.

Using simple mathematics, it can be shown that the ratio of rms to geometric average of nonlinear responses divided by their elastic counterparts is almost always greater than one and that it tends to one for long periods. This trend is confirmed in Figure 15, which shows q_{avg} computed for a constant-strength level $R = 4$ for the real records and for each of the five synthetic datasets mentioned above. Therefore, the effect of using the geometric mean rather than the rms mean is expected to have a noticeable effect only in the short period range.

Replacing the rms mean with the geometric mean when computing the inelastic-to-elastic median spectral ratios makes these ratios slightly closer to unity in the short period range than the ratios shown in top panels of Figures 5 to 7. The effect of using the geometric instead of the rms mean decreases with increasing R value such that this difference almost disappears for $R=10$. Figure 16, which is analogous to top panel of Figure 5, shows the case where the effect of the averaging technique is largest¹³. Note that at periods above approximately 0.5s the component averaging technique has no effect on the assessment of the median response at all the structural strengths considered here.

¹³ Beresnev and Silva provided only one component per station. The curves for the Beresnev and Silva models in Figures 4 and 15 are different because the different averaging technique affects the computation of the normalizing factor that uses two components of the real records.

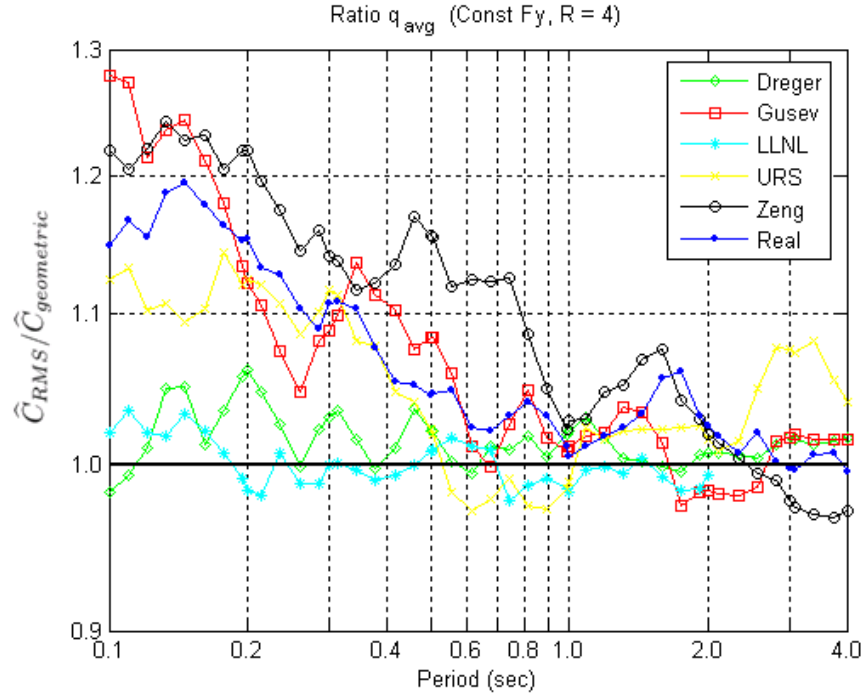


Figure 15: Ratio q_{avg} based on constant-strength analysis ($R = 4$). See Eq. (3) for the definition of q_{avg} . Note that only those datasets that contained component pairs of records at each recording station are shown.

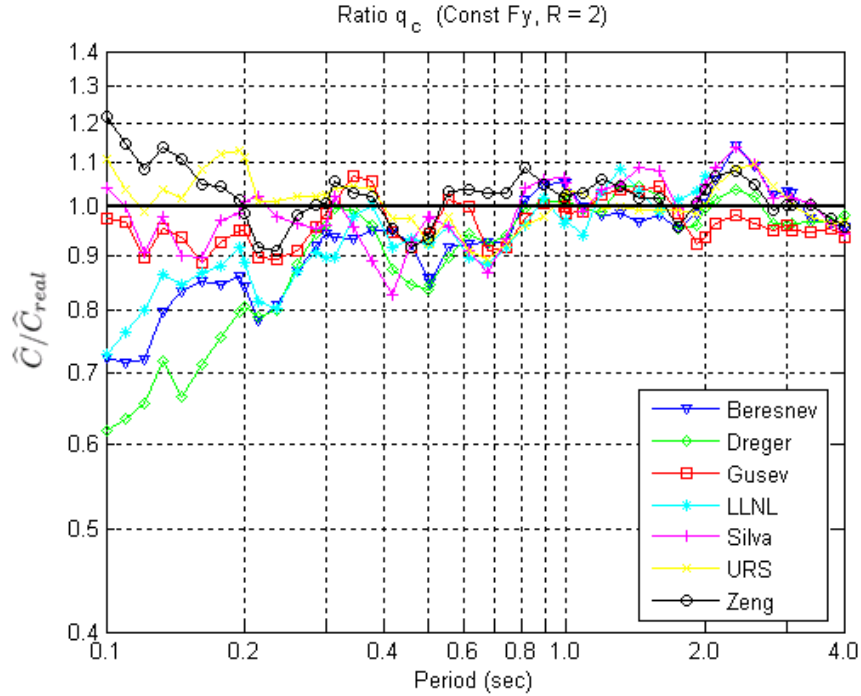


Figure 16: Ratio of the medians of the inelastic-to-elastic spectral ratio, C , for the seven synthetic datasets normalized by the corresponding quantity, C_{real} , obtained from the suite of real records. Both C and C_{real} were computed for a level of inelasticity defined by $R=2$ using the geometric mean of the responses to the two horizontal components, when available. The difference between averaging techniques decreases with increasing period and increasing R . This figure should be inspected in conjunction with the top panel of Figure 5.

4.3 Influence of Yield Strength Definition

All the results shown so far were computed for SDOF systems with constant strength (or constant yield force, F_y) for all the records. Therefore, as mentioned earlier, the value of R referred to above applies only in an average sense for all the records and not necessarily for each single record. Alternatively, we could keep a constant- R for all the records by appropriately modifying F_y for each one. The choice of preferring a constant-strength to a constant- R approach is, of course, entirely subjective. Other analysts could prefer the use of the constant- R approach instead. To assess whether the results that were shown so far still hold for the constant- R case, we investigated the statistical differences in the two following quantities, q_c and q'_c :

$$q_c = \left(\frac{C}{C_{real}} \right)_{Const-F_y} ; \quad q'_c = \left(\frac{C}{C_{real}} \right)_{Const-R} \quad (4)$$

The graphs of q_c for $R=2, 4$, and 10 were shown in the top panels of Figures 5 to 7. The computed values of the ratio q'_c/q_c are shown in Figure 17a, 17b, and 17c for $R = 2, 4$ and 10 , respectively. This ratio, which is clearly both model-dependent and R -dependent, can be significantly different than unity. This translates into potentially different systematic differences between nonlinear responses generated by the real dataset and the synthetic ones if the constant- R definition rather than the constant-strength definition is adopted.

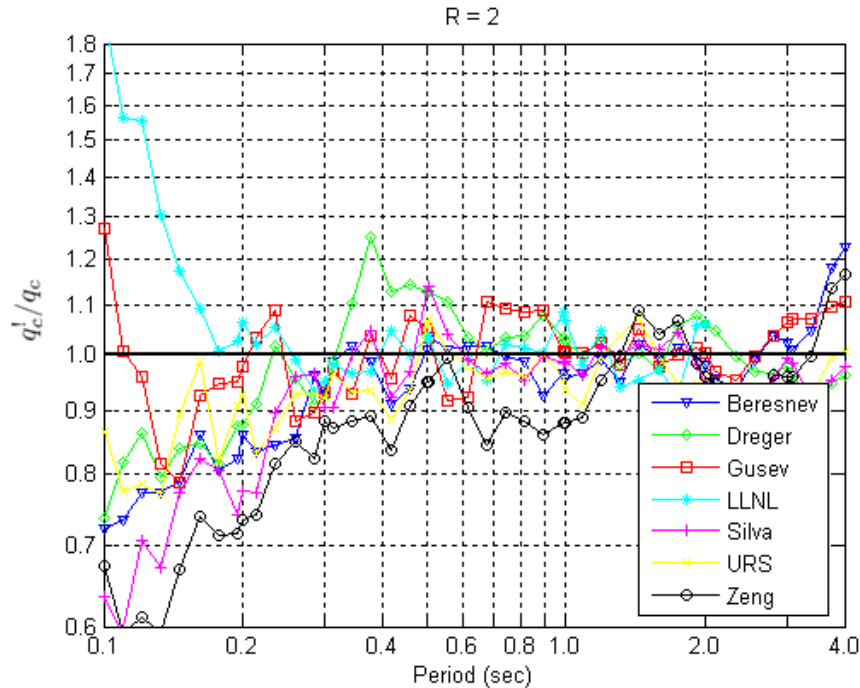


Figure 17a: Trend of the q'_c/q_c curves computed for $R=2$ for the seven simulation models. Note that q'_c refers to the constant- R results while q_c refers to the constant-strength results that have been discussed throughout the report. See Eq. (4) for the definitions of q_c and q'_c .

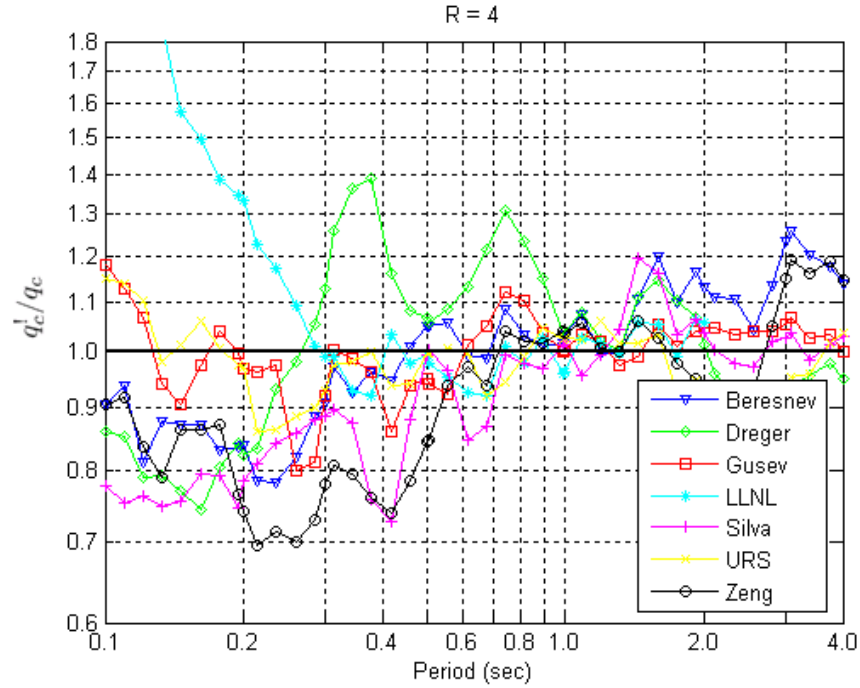


Figure 17b: Trend of the q'_c/q_c curves computed for $R=4$ for the seven simulation models. Note that q'_c refers to the constant-R results while q_c refers to the constant-strength results that have been discussed throughout the report. See Eq. (4) for the definitions of q_c and q'_c .

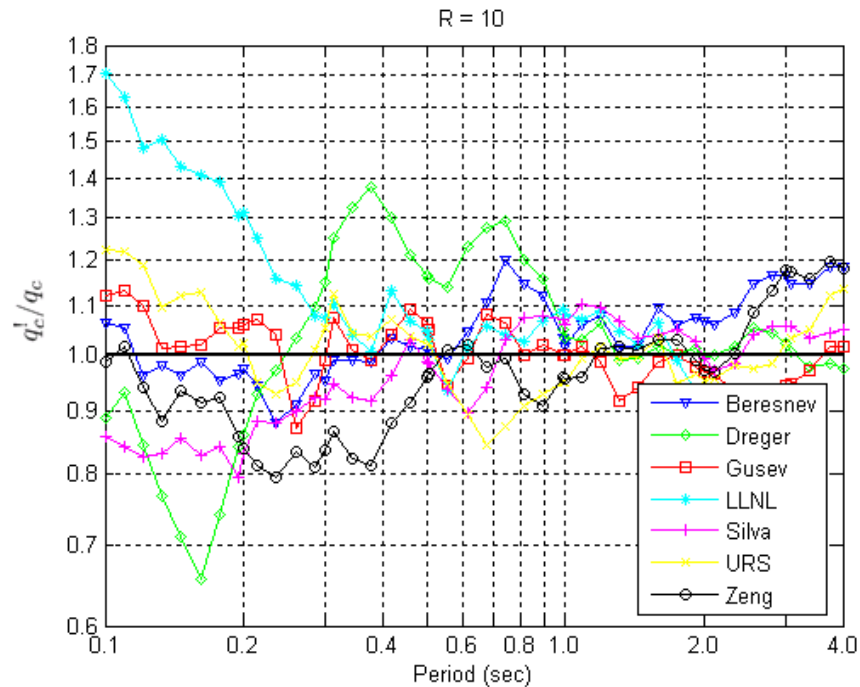


Figure 17c: Trend of the q'_c/q_c curves computed for $R=10$ for the seven simulation models. Note that q'_c refers to the constant-R results while q_c refers to the constant-strength results that have been discussed throughout the report. See Eq. (4) for the definitions of q_c and q'_c .

To quantify the extent of such differences, if any, we repeated all the nonlinear response analyses using the constant-R definition for all the datasets, both real and synthetic. The effect on the confidence limits for q'_c of using this alternative R definition is shown in Figures 18 to 24. These graphs should be compared with those in Figures 8 to 14. From inspecting this second batch of plots one can conclude that none of the conclusions that applied to the constant-strength approach are significantly affected by the adoption of the constant-R approach to the yield strength definition. The major differences affect the model by LLNL, that becomes unbiased for $R=2$ and 4 across the entire period range, and both the models by Silva and Zeng, whose amounts of bias are slightly worsened.

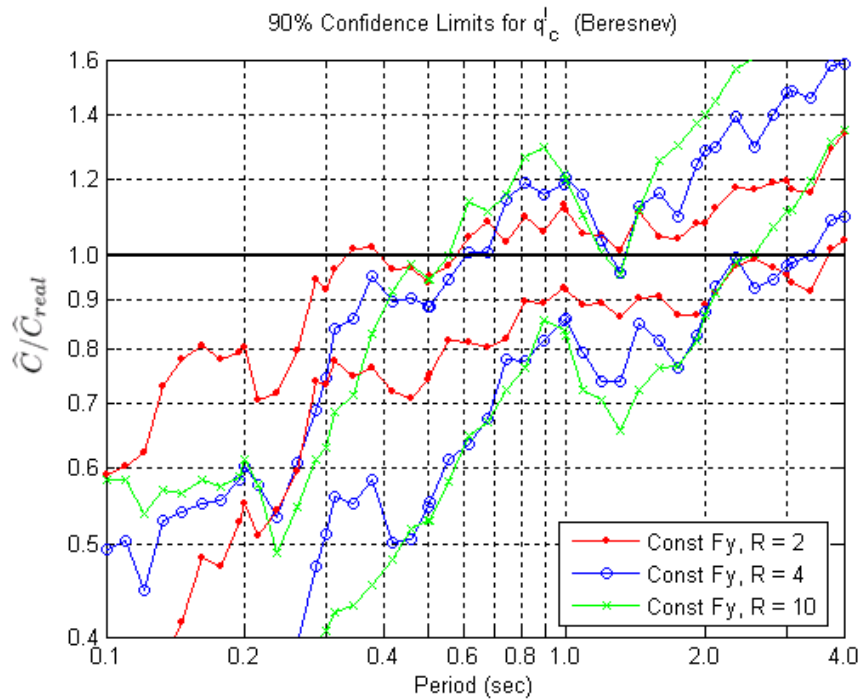


Figure 18: Upper and lower 90% confidence limits for q'_c for constant-strength levels $R = 2, 4$ and 10 for the Beresnev model. The ratio is significantly different than one at those periods where the unity line is not bracketed by the lower and upper bounds of the confidence band. Compare these confidence limits with those computed using the constant-strength approach (Figure 8).

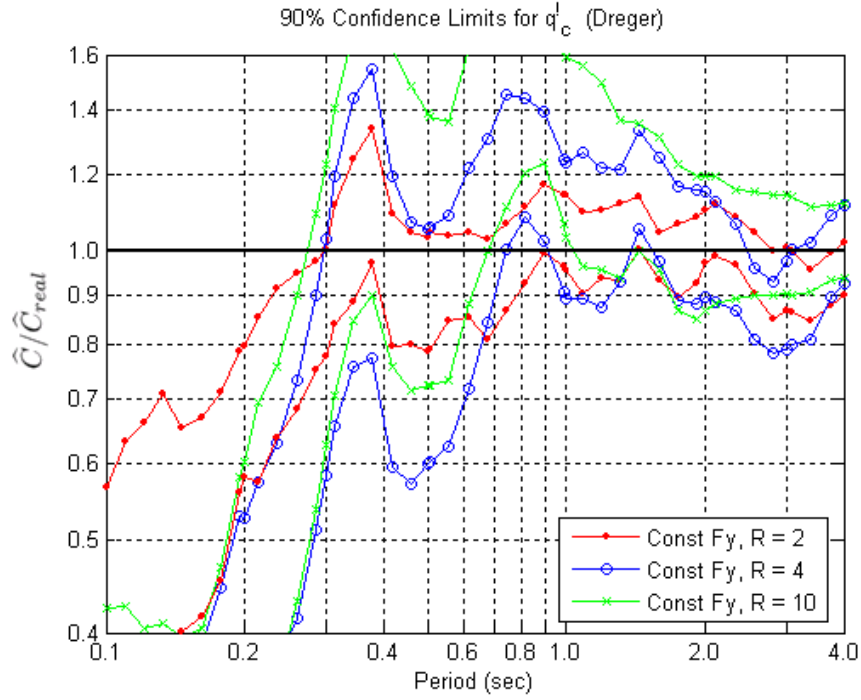


Figure 19: Upper and lower 90% confidence limits for q'_c for constant-strength levels $R = 2, 4$ and 10 for the Dreger model. The ratio is significantly different than one at those periods where the unity line is not bracketed by the lower and upper bounds of the confidence band. Compare these confidence limits with those computed using the constant-strength approach (Figure 9).

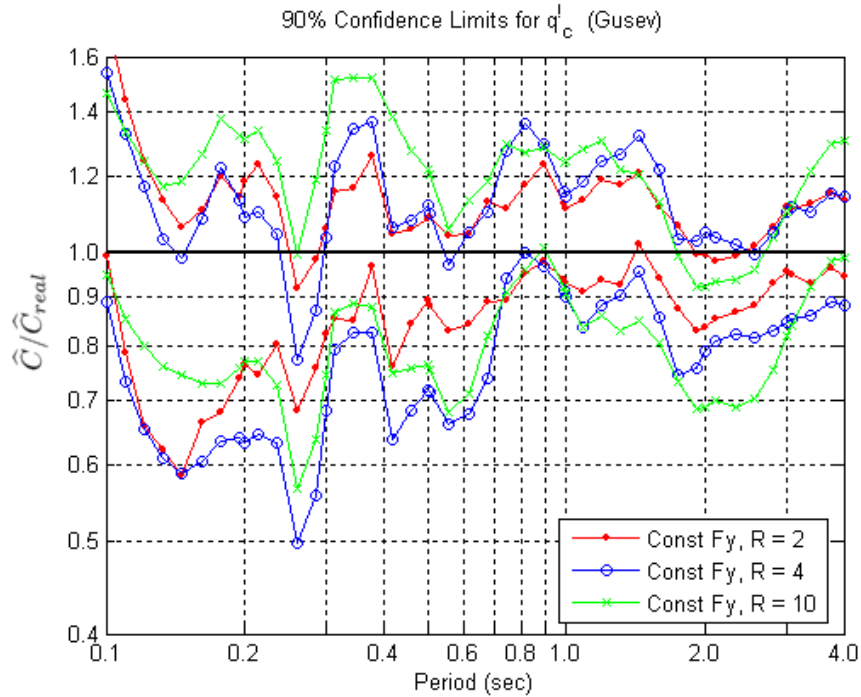


Figure 20: Upper and lower 90% confidence limits for q'_c for constant-strength levels $R = 2, 4$ and 10 for the Gusev model. The ratio is significantly different than one at those periods where the unity line is not bracketed by the lower and upper bounds of the confidence band. Compare these confidence limits with those computed using the constant-strength approach (Figure 10).

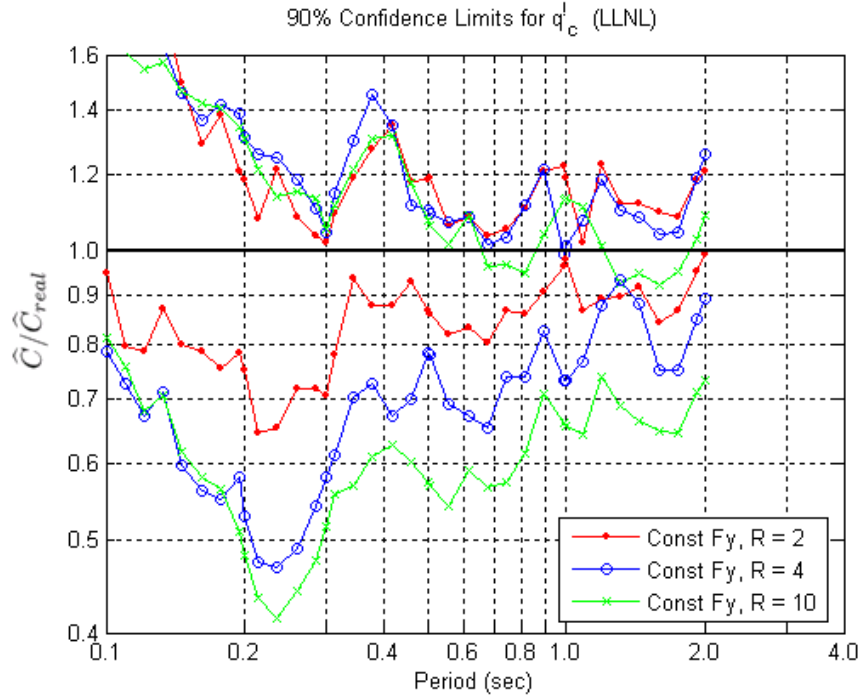


Figure 21: Upper and lower 90% confidence limits for q'_c for constant-strength levels $R = 2, 4$ and 10 for the LLNL model. The ratio is significantly different than one at those periods where the unity line is not bracketed by the lower and upper bounds of the confidence band. Compare these confidence limits with those computed using the constant-strength approach (Figure 11).

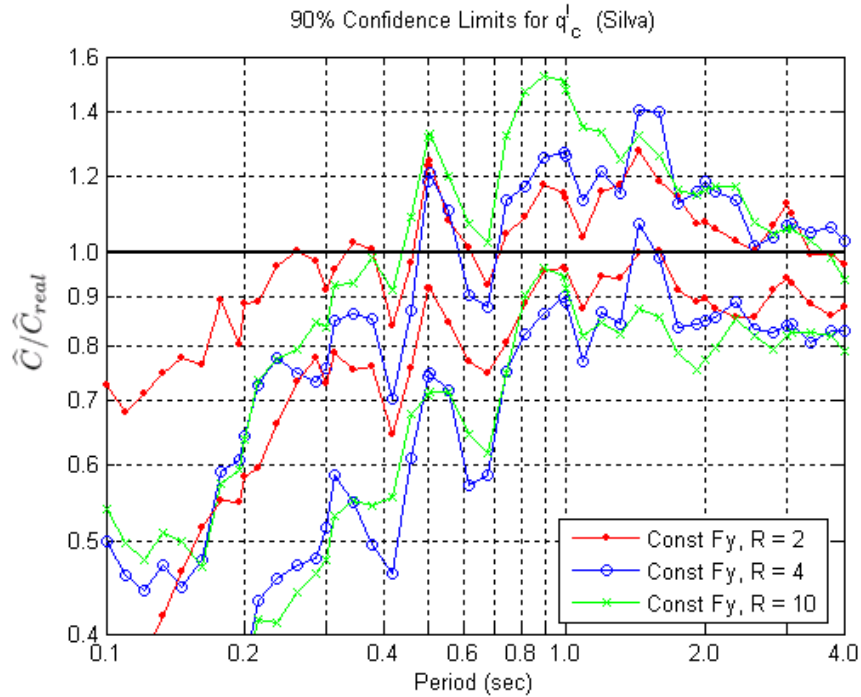


Figure 22: Upper and lower 90% confidence limits for q'_c for constant-strength levels $R = 2, 4$ and 10 for the Silva model. The ratio is significantly different than one at those periods where the unity line is not bracketed by the lower and upper bounds of the confidence band. Compare these confidence limits with those computed using the constant-strength approach (Figure 12).

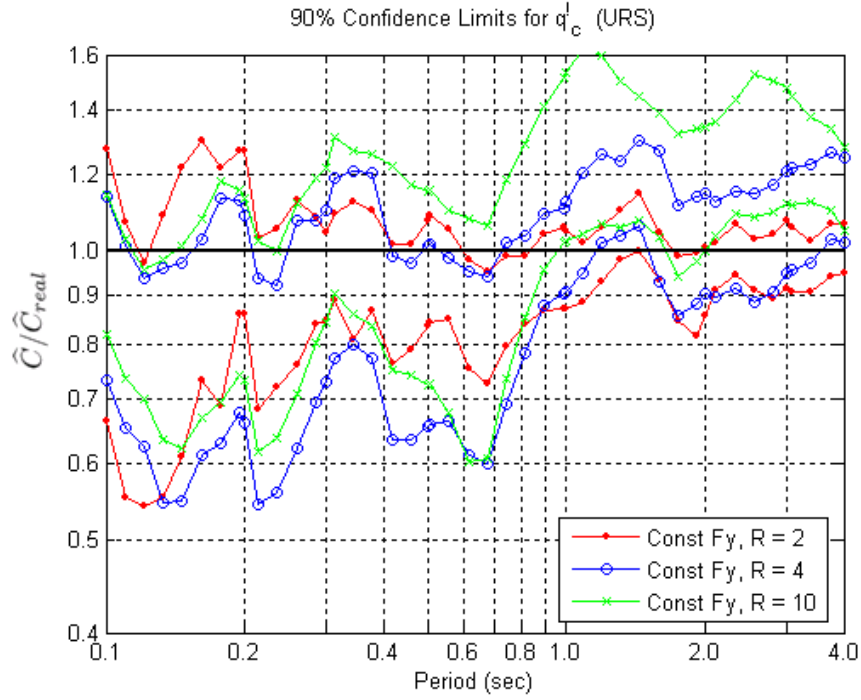


Figure 23: Upper and lower 90% confidence limits for q'_c for constant-strength levels $R = 2, 4$ and 10 for the URS model. The ratio is significantly different than one at those periods where the unity line is not bracketed by the lower and upper bounds of the confidence band. Compare these confidence limits with those computed using the constant-strength approach (Figure 13).

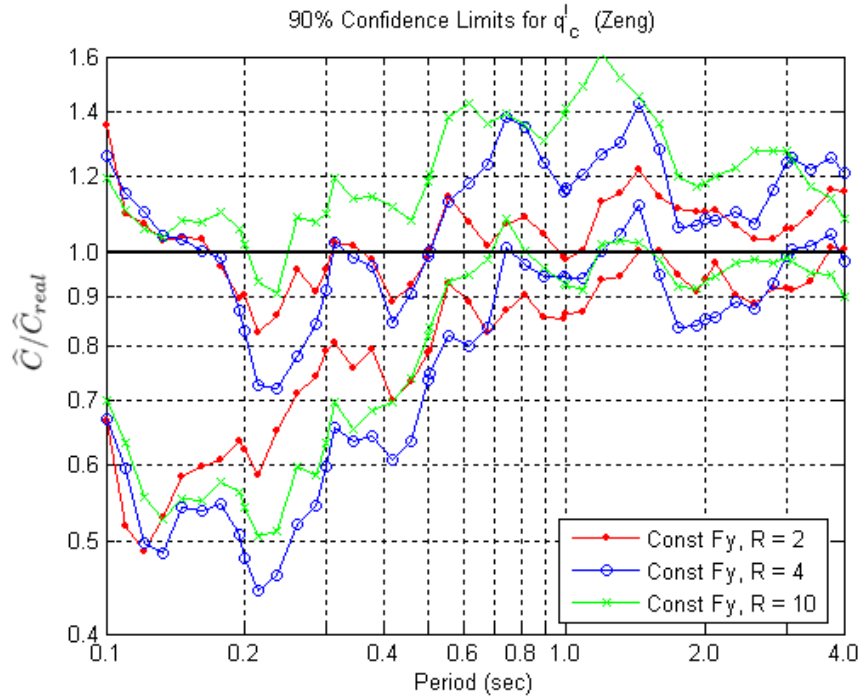


Figure 24: Upper and lower 90% confidence limits for q'_c for constant-strength levels $R = 2, 4$ and 10 for the Zeng model. The ratio is significantly different than one at those periods where the unity line is not bracketed by the lower and upper bounds of the confidence band. Compare these confidence limits with those computed using the constant-strength approach (Figure 14).

4.4 Effects on Nonlinear Responses Measured by Energy-Based Parameters

An alternative to quantifying the nonlinear dynamic response of a structure by a peak measure such as spectral displacement involves the use of a cumulative energy-based measure, such as input energy (E_i) or absorbed energy (E_a). Some researchers prefer the use of cumulative rather than peak response measures because they are supposed to capture the effects of both strength and stiffness degradation and the ground motion duration. These energy parameters are determined by integrating the equation of motion with respect to the relative structural displacement (u). The energy balance form of the equation of motion is given by:

$$\frac{m(\dot{u}_t)^2}{2} + \int_0^t c \dot{u} du + \int_0^t f_s du = \int_0^t m \ddot{u}_t du_g \quad (5)$$

where u_t is the total structural displacement, f_s is the structural restoring force, u_g is the ground displacement, m is the system mass and c is the system damping. The first term in (5) is the *absolute* kinetic energy (E_k) at time t , the second term is the damping energy (E_d), the third term is the absorbed energy (E_a), and the right-hand side of (5) is the *absolute* input energy (E_i). An alternative form of (5) may also be derived in terms of the *relative* kinetic and input energy, which can differ significantly from their *absolute* counterparts for extremely long and short period structures (Uang and Bertero, 1988). In the period range considered here the difference between absolute and relative quantities is negligible.

Before plunging into performing additional nonlinear dynamic analyses, we investigated the correlation between the response quantity used so far, namely the spectral displacement, S_d , and E_i or E_a to determine if an energy-based parameter is likely to provide additional insight into nonlinear response bias associated with the ground motion simulation techniques. In this correlation study, we considered the equivalent velocity form of the two energy parameters. The input energy-equivalent velocity (V_i) and absorbed energy-equivalent velocity (V_a) were chosen because they are commonly used energy measures for which attenuation models have been developed (Lawson, 1996; Chou and Uang, 2000). The equations for the energy-equivalent velocities are given by:

$$V_i = \sqrt{\frac{2(E_i)_{\max}}{m}} \quad ; \quad V_a = \sqrt{\frac{2(E_a)_{\max}}{m}} \quad (6)$$

where m is the mass of the SDOF structure. Note that in the case of elastic analysis, the absorbed energy-equivalent velocity (V_a) converges to the pseudo-velocity of the SDOF system.

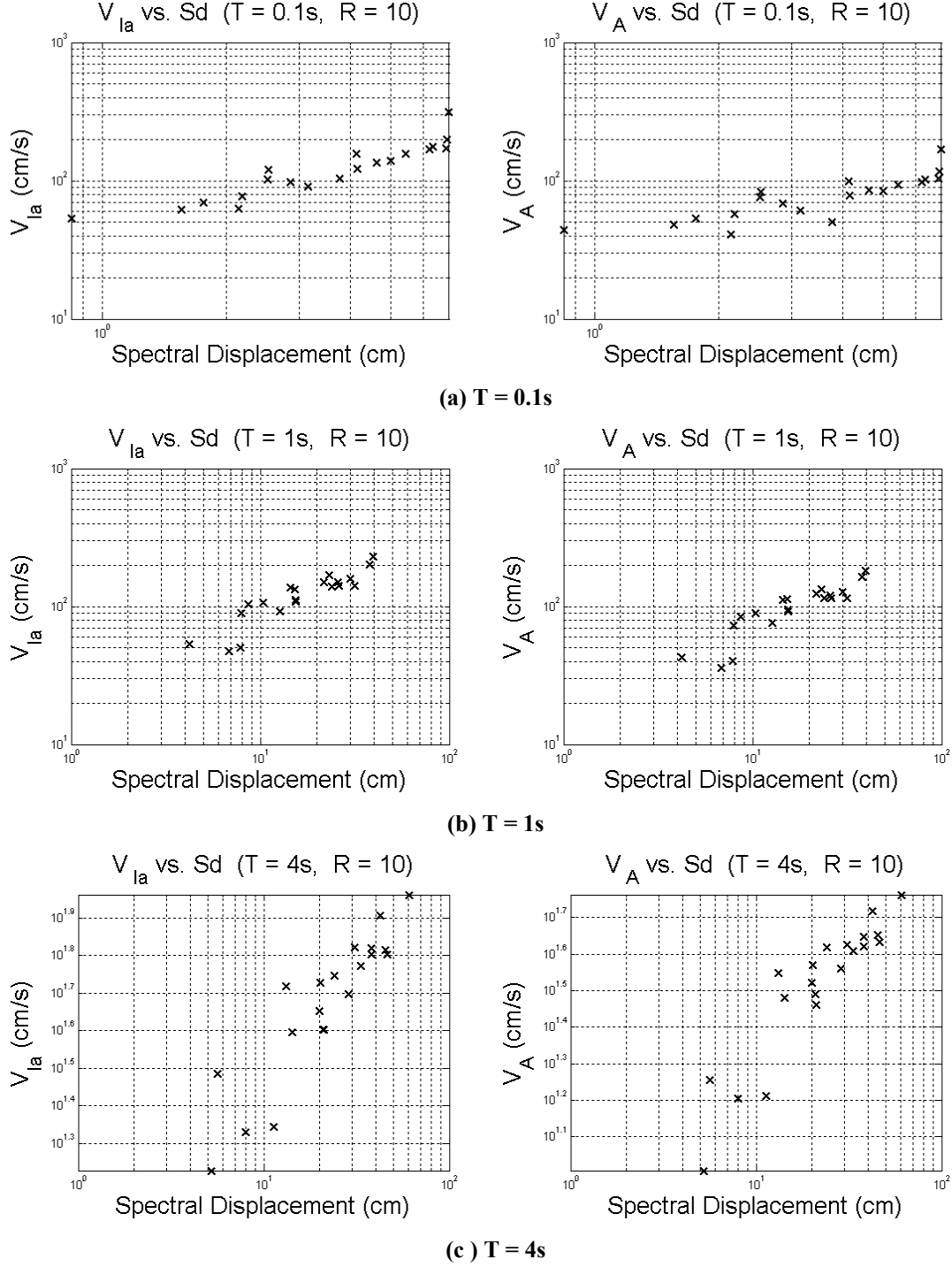


Figure 25: Correlation between spectral displacement and both *absolute* input energy-equivalent velocity (V_i) (figures on the left) and absorbed energy-equivalent velocity (V_a) (figures on the right) for the twenty real records and constant-strength $R = 10$ at $T = 0.1s$, $1s$, and $4s$.

The three figures on the left-hand side of Figure 25 show the relationship between spectral displacement and *absolute* V_i for the twenty real records and constant-strength R equal to 10 at a structural periods of 0.1s (Panel a), 1s (Panel b), and 4s (Panel c).

Similar relationships between S_d and the absorbed energy-equivalent velocity, V_a , are displayed on the right-hand side of the same figure. The lowest constant-strength corresponding to $R=10$ was chosen to ensure that each of the twenty records produced significant nonlinear response to avoid mixing elastic and inelastic behavior in the computed absorbed energy results. It is apparent from Figure 25 that a strong linear relationship (i.e., correlation coefficients range from 0.84 to 0.92) exists between spectral displacement and each energy-equivalent velocity parameter. Hence, an investigation of nonlinear response bias associated with synthetic ground motion time histories using an energy-based parameter would most likely not bring any additional insights. One can conclude that the systematic differences between energy-based nonlinear responses computed by synthetic and real records are similar to those shown in the Figures 5 to 14.

5.0 Inelastic Response Spectra for NGA¹⁴ Database and Related Software

Developers of synthetic ground motions may have the need to test on their own whether the nonlinear responses of SDOF oscillators subject to simulated ground motions are in agreement with those produced by real records for the same earthquake scenario. To help this effort we are going to compute the *nonlinear displacement response spectra* for $R=2,4,6,8$, and 10 for all the records in the soon-to-be-developed NGA database. The horizontal components of this database are rotated into the two directions normal and parallel to the fault strike. The spectra will be computed for 5%-damped nonlinear Single-Degree-of-Freedom (SDOF) oscillators with natural periods ranging from 0.1 to 4.0s, a bilinear backbone force-deformation curve with 5% post-yield hardening¹⁵, and a hysteretic rule that has no degradation of either strength or stiffness. The nonlinear displacement response spectra will be provided in the same format as that used in the NGA project to store the elastic pseudo-acceleration response spectra for the same records. Also, we will provide a MATLAB subroutine to assist in the computation of nonlinear response spectra for additional records not included in this database.

Both the nonlinear spectra and the MATLAB subroutine with instructions for its use will be provided to PEER immediately after the NGA database is made available to us.

6.0 Conclusions

This study has investigated whether ground motion simulation techniques produce *nonlinear* displacement response spectra that are statistically distinguishable from those created by real records. The spectra were computed for nonlinear SDOF systems with bilinear backbone curves and no degrading stiffness or strength, a hardening ratio of 2%, and periods ranging from 0.1s to 4.0s. The level of response nonlinearity was defined by different levels of the force reduction factor, R , ranging from two (mild nonlinearity) to

¹⁴ Next Generation Attenuation (NGA) Relationships Project funded by the PEER Lifelines Program.

¹⁵ Note that in this study we have used SDOF systems with only 2% of post-yield hardening. The nonlinear displacement response spectra, however, will be provided for 5% hardening ratio rather than 2%. This choice is made to be consistent with a currently ongoing research project at Stanford University that is set to develop an attenuation relationship for S_d for SDOF systems with 5% hardening.

ten (severe nonlinearity). The investigation was done by means of a case study that used real accelerograms of the Northridge earthquake recorded at 20 stations located within 20km of the fault rupture. The nonlinear responses of the real records were considered as the target for the responses produced by the synthetic records that were provided by seven groups of seismologists. The comparisons were performed using the “average” of the responses generated by the two horizontal components at each station.

The agreement between elastic responses from records generated by these seven models and those from the real recordings for this case study has been thoroughly considered in another PEER-funded Project K201. We limit ourselves to saying here that six out of seven models were found to produce *elastic* spectra that have systematic deviations of different severity from the elastic spectra of real records, mostly (but not only) at short periods. The synthetic records seem to be more aggressive than those in nature in this period range. The deviations are statistically significant at the 10% level.

The core of this study, however, deals with the issue of whether any systematic deviations can be detected in the *post-elastic nonlinear* regime under the assumption that the elastic responses of real and synthetic records are in statistical agreement. To separate the elastic from the post-elastic nonlinear results, we considered the ratio of nonlinear to linear responses as the quantity to investigate for possible statistical discrepancies in the results generated by the synthetic models compared to those from real records. We found, again, that six out of seven models produced statistically biased nonlinear response spectra at least at some periods. Again, the systematic deviation, which is significant with 90% confidence, is more prominent at lower periods and at larger R values. Unlike the elastic case, however, the synthetic records tend to be more benign than real ones in producing nonlinear responses in stiff structures especially in the severe nonlinear range. One model, however, produces records that at long periods generate nonlinear responses for $R=10$ that are more severe than those from real records. The reason for the deficiency in the *nonlinear* responses to synthetic records at short periods lies in the difference that, on average, exists between the *linear* response spectra of these synthetic records and those of real ones in that period range. When the response of an SDOF system becomes severely nonlinear, its effective vibration period lengthens significantly and, therefore, it becomes dependent on the frequency content of the record in a fairly large bandwidth and not only in the neighborhood of the initial elastic natural period of vibration.

Besides the possible bias in the assessment of nonlinear structural responses introduced by the use of simulated records, we also compared the variability of nonlinear responses generated by simulated and real records. Most of these models appear to underestimate the record-to-record response variability from real records at shorter periods and, for high level of nonlinearity (e.g., $R \geq 4$) only, to overestimate it at longer periods. A more limited variability may become useful in practice when one wants to assess the median response of structures because, once any bias is corrected, the same accuracy can be achieved with fewer runs involving synthetic rather than real records. However, nonlinear response variability for simulated records lower or higher than that for real records can affect the safety assessment of structures against collapse, for example. Collapse probability

estimates are controlled by extreme response values, and if they are less likely to occur for synthetic than for real records, such as it seems for some of the models in the short period range, then the “true” collapse probability would be underestimated and the safety assessment possibly misguided.

These conclusions about systematic differences in nonlinear responses from synthetic and real records were tested by evaluating their sensitivity to a) a two different schemes of averaging the ground motion horizontal components, b) to an alternative definition of R , and c) to the use of a cumulative energy-based ground motion parameter rather than peak displacement. We detected some differences but the conclusions were found to be sufficiently robust to all three of these tests.

We must emphasize, however, that all the conclusions drawn here were based on one case study involving only 20 stations and one earthquake. They may not apply to other cases and/or other simulation techniques. More research should be done to test the validity of these conclusions with additional test cases.

Acknowledgements

The authors are deeply indebted to the developers of the synthetic ground motion records for allowing their use in this comparative study. The help provided by Prof. Pedro de Alba in coordinating the release of the records and of the support information is also gratefully acknowledged. Finally, we are very thankful to Dr. Norman Abrahamson, Dr. Brian Chiou, and Cliff Roblee for their constant support that made this study possible. The PEER Lifelines Program provided the funding for this study.

References

- Abrahamson, N.A., and Silva, W.J. (1997), “Empirical Response Spectral Attenuation Relations for Shallow Crustal Earthquakes”, *Seismological Research Letters*, 68(1), 94-127.
- Chou, C.C., and Uang, C.M. (2000), “An Evaluation of Seismic Energy Demand: An Attenuation Approach”, PEER Report 2000/04, Univ. of California, Berkeley, California.
- Lawson, R.S. (1996), “Site-Dependent Inelastic Seismic Demands”, Ph.D. Thesis, Stanford Univ., Stanford, California.
- Uang, C.M., and Bertero, V.V. (1988) “Use of Energy as a Design Criterion in Earthquake-Resistant Design”, Rep. No. UCB/EERC-88/18, Earthquake Engineering Research Center, Univ. of California, Berkeley, California.
- Veletsos AS, Newmark NM. (1960). “Effect of inelastic behavior on the response of simple systems to earthquake motions”, *Proceedings of the 2nd World Conference on Earthquake Engineering*, Japan, vol. 2, 1960; 895–912.

Appendix A: Simulation Methodologies

Modeler 1: Dr. Igor Beresnev

Simulation of records for the Northridge earthquake was performed using the stochastic finite-fault ground-motion modeling technique. In the method, the fault plane is discretized into rectangular elements (subfaults), each of which is treated as a point source and assigned an average ω^{-2} spectrum with a stochastic component superimposed on it, in the same manner as for the stochastic point sources introduced by Boore (1983). The total number of subfaults is prescribed by the seismic moment of the target event. The rupture starts at the hypocenter and propagates radially outward with a prescribed constant velocity, triggering subsources as it reaches them. Subsource trigger times are randomized. The generated subfault acceleration time history is propagated to the observation point using empirical (distance-dependent) duration, geometric-attenuation, and anelastic-attenuation (Q) models, which are user-defined and thus can be adjusted to any specific region. The contributions from all subsources are summed up in the time domain at the observation point, with proper delays accounting for the propagation-distance differences. Site effects can be introduced by specifying a site amplification function and an Anderson-Hough low-pass filtering parameter “kappa”.

The subfault size in the method is chosen from the empirical model established from the method calibration on 26 large earthquakes,

$$\log \Delta l = -2 + 0.4 \mathbf{M}, 4 \leq \mathbf{M} \leq 8,$$

where \log is base 10, Δl is the subfault linear dimension in km, and \mathbf{M} is the moment magnitude of the target event (Beresnev and Atkinson, 2002, equation 1). The only free parameter of the simulations is the maximum-slip velocity on the fault, which reflects parametric variability in ground-motion predictions for future events.

The method is implemented in the FORTRAN code FINSIM (Beresnev and Atkinson, 1998a). The details of the technique and the results of its multiple calibrations are fully described in a series of publications by the authors (Beresnev and Atkinson, 1997, 1998a,b, 1999, 2002).

References

- Beresnev, I. A. and G. M. Atkinson (1997). Modeling finite-fault radiation from the ω^n spectrum, *Bull. Seism. Soc. Am.* **87**, 67-84.
- Beresnev, I. A. and G. M. Atkinson (1998a). FINSIM - a FORTRAN program for simulating stochastic acceleration time histories from finite faults, *Seism. Res. Lett.* **69**, 27-32.
- Beresnev, I. A. and G. M. Atkinson (1998b). Stochastic finite-fault modeling of ground motions from the 1994 Northridge, California, earthquake. I. Validation on rock sites, *Bull. Seism. Soc. Am.* **88**, 1392-1401.
- Beresnev, I. A. and G. M. Atkinson (1999). Generic finite-fault model for ground-motion prediction in eastern North America, *Bull. Seism. Soc. Am.* **89**, 608-625.
- Beresnev, I. A. and G. M. Atkinson (2002). Source parameters of earthquakes in eastern and western North America based on finite-fault modeling, *Bull. Seism. Soc. Am.* **92**, 695-710.
- Boore, D. M. (1983). Stochastic simulation of high-frequency ground motions based on seismological models of the radiated spectra, *Bull. Seism. Soc. Am.* **73**, 1865-1894.

Modeler 2: Dr. Douglas Dreger

The spatial and temporal description of fault slip from Wald *et al.* (1996) was used for Northridge record simulation. The Wald model is a multiple time window parameterization following the method of Hartzell and Heaton (1983), and the code for this model (Dreger and Kaverina, 2000; Kaverina et al., 2002) is the same. In the Wald model there are six time windows. Three describe how slip is released with time following the passage of a constant velocity rupture front, and for each time window there are two possible slip directions (55-degree and 145-degree (90 degrees apart)). The actual slip direction is the linear sum of these two components. The rise time and rupture velocity used by Wald to best fit the data were used in this model. The original set of ground motions assumed a triangular rise time function, and in the second set an omega-squared model was used. The second set is considered to be better since the records do not suffer from spectral nulls that the triangular function suffers from. I also assumed The 1D rock velocity model Wald specified was assumed in this model. Given the source parametric information and Green's functions from the 1D model the time histories were simulated by direct point-source summation where contributions from each of the subfaults for each time window and slip direction were delayed according to the rupture trigger time and summed. Non-rock sites were adjusted by multiplying by a factor representing the site amplification. Factors of 1.4 and 1.78 were used for NEHRP C and D sites, respectively. The factors were determined based on vertical SH wave amplification from the 1 km/s rock velocity to the corresponding NEHRP site velocities. The Wald *et al.* (1996) model is band limited due to their bandpass filtering of the data between 0.1 to 1 Hz.

References

- Dreger, D. S. and A. Kaverina (2000). Seismic remote sensing for the earthquake source process and near-source strong shaking: a case study of the October 16, 1999 Hector Mine earthquake, *Geophys. Res. Lett.*, 27, 1941-1944.
- Hartzell, S. H., and T. H. Heaton (1983). Inversion of strong ground motion and teleseismic waveform data for the fault rupture history of the 1979 Imperial Valley, California, earthquake, *Bull. Seism. Soc. Am.*, 73, 1553-1583.
- Kaverina, A., D. Dreger, and E. Price (2002) The combined inversion of seismic and geodetic data for the source process of the 16 October 1999 M (sub w) 7.1 Hector Mine, California, Earthquake, *Bull. Seism. Soc. Am.*, vol.92, no.4, pp.1266-1280.
- Wald, D. J., T. H. Heaton, and K. W. Hudnut (1996). The slip history of the 1994 Northridge, California, earthquake determined from strong-motion, teleseismic, GPS and leveling data, *Bull. Seism. Soc. Am.*, 86, s49-s70.

Modeler 3: Dr. Alexander Gusev *et al.*, Institute of Volcanic Geology and Geochemistry

The earthquake ground motion simulation technique in the model was developed by A.Gusev and V.Pavlov. It permits the simulation of realistic earthquake ground motions at a site and the ability to study the variability of such a motion. Eventually, a suite of design ground motions for scenario earthquake(s) may be generated. The technique combines a multiple-point-source version of a stochastic earthquake fault model and a suite of Green's functions calculated for layered weakly anelastic medium. The source model consists of a grid of point subsources with appropriate random time histories. A large number of properties/parameters of the simulated earthquake fault can be adjusted in order to: (1) tune the model to a particular seismological situation; and/or (2) to analyze the variability and uncertainties of strong motion prediction; or also (3) to generate a suite of motions that represents these uncertainties. These parameters consist of two large groups: (1) physical parameters that are fixed in a particular run of the simulator (their variation produces "parametric variability") and (2) "random" parameters that are essentially random seeds; they produce "model variability".

The source simulation module is based on the generalization of the classic Haskell (1966) stochastic fault model. Its important modifications are: (1) variable final slip governed by the power spectrum that is a power-law with respect to wave number; (2) circular rupture front with an arbitrary nucleation point and variable rupture velocity, random with a prescribed mean; (3) local slip velocity, or the moment rate of a subsurface, is random, with a common duration or rise time. The grid of subsources covers the rupture. Individual subsources have no geophysical meaning, its number is arbitrary, and can be large if the site in question is located at a small distance from a large-magnitude fault. Instead of Haskell's omega-cube far field spectrum, the far-field spectrum of a simulated source is adjusted, in its high-frequency part, to a particular, preset, average (regional) spectral scaling law.

To calculate the pulse response of the layered elastic medium from double-couple source for distances less than 50 km, a version of the method of Alekseev and Mikhailenko (1976) is used, developed by Pavlov (2002) who advanced the "auxiliary functions" approach first introduced by Fatyanov and Mikhailenko (1988). The main advantage of this method is the lack of numerical instability inherent within propagator methods, because in the auxiliary function method all relevant exponential factors are below unity by absolute value. To ensure preset uniform numerical accuracy, the number of terms in the series expansion is selected adaptively. The developed numerical method provides accurate broad-band representation of ground motions in a layered medium, from static terms to high frequencies.

References

- Alekseev A.S., Mikhilenko B.G. (1976). "Solution of Lamb problem for a vertically inhomogeneous elastic half-space", *Izv. Akad. Nauk USSR, Fizika Zemli*, 12, 11-25 (in Russian).
- Fatyanov A.G., Mikhilenko B.G. (1988). A technique for calculation of non-stationary seismic wave fields in inelastic layered media. *Dokl. Akad. Nauk USSR*, 301, 834-839 (in Russian).
- Pavlov V., (2002). "A convenient technique for calculating synthetic seismograms in a layered half-space". *Proceedings of the 4th International Conference "Problems of Geocosmos"*, St. Petersburg, pp. 320-323.

Modeler 4: Dr. Lawrence Hutchings et al., LLNL

We numerically compute the discretized representation relation in a form that utilizes analytical slip functions and empirical or synthetic Green's functions. We derive rupture models that are consistent with physical understanding of how earthquakes rupture. An important claim in this approach is that we use physical and measurable parameters, so that they can be identified and bounded in a prediction. Discretization is small enough (for elemental areas) and short enough (for time steps) to model continuous rupture to the highest frequency of interest. Empirical Green's functions are obtained from recordings of small earthquakes with effectively a step-source time functions, and are adjusted for source location and focal mechanism solution to model the Green's function from each elemental area. We often use synthetic Green's functions for low frequencies, but we did not do that for this exercise. Rupture parameters include rupture geometry, hypocenter, rupture roughness, rupture velocity, healing velocity, Kostrov slip function, asperity size and location, and slip vector. Slip follows the Kostrov slip function for the time required for the rupture front to reach the fault edge from the hypocenter and for a healing phase to reach an element from the fault edge. We used a rupture velocity of 2.9 km/sec and a healing velocity of 2.3 km/s. Asperities are modeled as areas with high slip amplitudes and high stress drop. Fault displacement for asperities grade from the value of background rupture at the edge to greatest at the center. Stress drop is a dependent variable derived from the Kostrov slip function; for this exercise it has a value of 180 bars for the non-asperity portion of rupture, and between 300 and 600 bars for asperities. Stress drop also diminishes near the surface at the rate of the lithostatic load. Rupture roughness is modeled by a percentage of elemental areas having rise time randomly shortened to between 0.1 and 0.9 times the original value. Roughness is implemented by delaying an element's rupture time so that it finishes slip at the same time as neighboring elements. Elements with rough rupture have higher stress drop. In our model of the Northridge earthquake 20% of the elements had rough rupture. Our model of the Northridge earthquake was previously published (Hutchings, 1994) and utilized previously published reports of fault geometry, hypocenter, slip vector, and slip distribution. We did not iterate around rupture parameters to find the best fit to observed seismograms for this exercise.

References

Hutchings, L. (1994). "Kinematic earthquake models and synthesized ground motion using empirical Green's functions, *B.S.S.A.*, Vol 84, No. 4, pp. 1028-1050.

Modeler 5: Dr. Walter Silva

STOCHASTIC FINITE-SOURCE MODEL GROUND MOTION MODEL

In the near-source region of large earthquakes, aspects of a finite-source including rupture propagation, directivity source-receiver geometry, and saturation of high-frequency (≥ 1 Hz) motions with increasing magnitude can be significant and may be incorporated into strong ground motion predictions. To accommodate these effects, a methodology that combines the aspects of finite-earthquake-source modeling techniques (Hartzell, 1978; Irikura 1983) with the stochastic point-source ground motion model has been developed to produce response spectra as well as time histories appropriate for engineering design (Silva et al., 1990; Silva and Stark, 1993; Schneider et al., 1993). The approach is very similar to the empirical Green function methodology introduced by Hartzell (1978) and Irikura (1983). In this case however, the stochastic point-source is substituted for the empirical Green function and peak amplitudes; PGA, PGV, and response spectra (when time histories are not produced) are estimated using random process theory.

Use of the stochastic point-source as a Green function is motivated by its demonstrated success in modeling ground motions in general and strong ground motions in particular (Boore, 1983, 1986; Silva and Stark, 1993; Schneider et al., 1993; Silva and Darragh, 1995) and the desire to have a model that is truly site- and region-specific. The model can accommodate a region specific $Q(f)$, Green function sources of arbitrary moment or stress drop, and site specific kappa values and soil profiles. The necessity for having available regional and site specific recordings distributed over the rupture surface of a future earthquake or modifying possibly inappropriate empirical Green functions is eliminated.

For the finite-source characterization, a rectangular fault is discretized into NS subfaults of moment M_0^S . The empirical relationship

$$\log (A) = \mathbf{M} - 4.0, \quad A \text{ in km}^2 \quad (\text{A1})$$

is used to assign areas to both the target earthquake (if its rupture surface is not fixed) as well as to the subfaults. This relation results from regressing log area on \mathbf{M} using the data of Wells and Coppersmith (1994). In the regression, the coefficient on \mathbf{M} is set to unity which implies a constant static stress drop of about 30 bars. This is consistent with the general observation of a constant static stress drop for earthquakes based on aftershock locations (Wells and Coppersmith 1994). The static stress drop, defined by Equation A4, is related to the average slip over the rupture surface as well as rupture area. It is theoretically identical to the stress drop which defines the omega-square source corner frequency assuming the rupture surface is a circular crack model (Brune, 1970; 1971). The stress drop determined by the source corner frequency (or source duration) is usually estimated through the Fourier amplitude spectral density while the static stress drop uses the moment magnitude and an estimate of the rupture area. The two estimates for the same earthquake seldom yield the same values with the static generally being the smaller. In a recent study (Silva et al., 1997), the average stress drop based on Fourier amplitude spectra determined from an empirical attenuation relation (Abrahamson and Silva, 1997) is about 70 bars while the average static stress drop for the crustal earthquakes studied by Wells and Coppersmith (1994) is about 30 bars. These results reflect a general factor of about 2 on average between the two values. These large differences may simply be the result of using an inappropriate estimate of rupture area as the zone of actual slip is difficult to determine unambiguously. In general however, even for individual earthquakes, the two stress drops scale

similarly with high static stress drops (> 30 bars) resulting in large high frequency (> 1 Hz for M_5) ground motions which translates to high corner frequencies.

The subevent magnitude M_S is generally taken in the range of 5.0-6.5 depending upon the size of the target event. M_S 5.0 is used for crustal earthquakes with M in the range of 5.5 to 8.0 and M_S 6.4 is used for large subduction earthquakes with $M > 7.5$. The value of NS is determined as the ratio of the target event area to the subfault area. To constrain the proper moment, the total number of events summed (N) is given by the ratio of the target event moment to the subevent moment. The subevent and target event rise times (duration of slip at a point) are determined by the equation

$$\log \tau = 0.33 \log M_0 - 8.54 \quad (A2)$$

which results from a fit to the rise times used in the finite-fault modeling exercises, (Silva et al., 1997). Slip on each subfault is assumed to continue for a time τ . The ratio of target-to-subevent rise times is given by

$$\frac{\tau}{\tau} = 10^{0.5(M-M_S)} \quad (A3)$$

and determines the number of subevents to sum in each subfault. This approach is generally referred to as the constant-rise-time model and results in variable slip velocity for nonuniform slip distributions. Alternatively, one can assume a constant slip velocity (as do Beresnev and Atkinson, 2002) resulting in a variable-rise-time model for heterogeneous slip distributions. This approach was implemented and validations resulted in an overall “best” average slip velocity of about 70 cm/sec, with no significant improvement over a magnitude dependent rise time (Equation A3). The feature is retained as an option in the simulation code.

Recent modeling of the Landers (Wald and Heaton, 1994), Kobe (Wald, 1996) and Northridge (Hartzell et al. 1996) earthquakes suggests that a mixture of both constant rise time and constant slip velocity may be present. Longer rise times seem to be associated with areas of larger slip with the ratio of slip-to-rise time (slip velocity) being depth dependent. Lower slip velocities (longer rise times) are associated with shallow slip resulting in relatively less short period seismic radiation. This result may explain the general observation that shallow slip is largely aseismic. The significant contributions to strong ground motions appear to originate at depths exceeding about 4 km (Campbell, 1993; Boore et al., 1994) as the fictitious depth term in empirical attenuation relation (Abrahamson and Silva, 1997; Boore et al., 1997). Finite-fault models generally predict unrealistically large strong ground motions for large shallow (near surface) slip using rise times or slip velocities associated with deeper (> 4 km) zones of slip. This is an important and unresolved issue in finite-fault modeling and the general approach is constrain the slip to relatively small values or rise time to large values in the top 2 to 4 km. For the composite source model, the approach is to taper the subevent stress drop to zero from a depth of 5 km to the ground surface (Yehua Zeng, personal communication 1999). This approach is also followed in the stochastic finite source model. For earthquakes with significant shallow slip, greater than 20% moment released in the top 5 km, expected short period ($< 1 - 2$ second) motions are significantly lower (20 – 50%) than those of deep slip events, of the same magnitude (Silva et al., 1997). To capture this effect, shallow slip earthquakes are modeled with a 5 bar, rather than 30 bar subevent stress drop, over the entire rupture surface, based on the validation exercises (Silva

et al., 1997). These results imply significantly different source processes affecting short periods between earthquakes which do not interact with low stresses associated with shallow rupture and those earthquakes which have deep rupture only. The implications to seismic hazard are obvious.

To introduce heterogeneity of the earthquake source process into the stochastic finite-fault model, the location of the sub-events within each subfault (Hartzell, 1978) are randomized as well as the subevent rise time ($\sigma_{in} = 0.8$). The stress drop of the stochastic point-source Green function is taken as 30 bars, consistent with the static value based on the **M** 5.0 subevent area using the equation

$$\Delta\sigma = \frac{7}{16} \left(\frac{M_e}{R_e^3} \right) \quad (\text{Brune, 1970, 1971}) \quad (\text{A4})$$

where R_e is the equivalent circular radius of the rectangular sub-event.

Different values of slip are assigned to each subfault as relative weights so that asperities or non-uniform slip can be incorporated into the methodology. For validation exercises, slip models are taken from the literature and are based on inversions of strong motion as well as regional or teleseismic recordings. To produce slip distributions for future earthquakes, random slip models are generated based on a statistical asperity model with parameters calibrated to the published slip distributions. This approach has been validated by comparing the modeling uncertainty and bias estimates for the Loma Prieta and Whittier Narrows earthquakes using motion at each site averaged over several (30) random slip models to the bias and uncertainty estimates using the published slip model. The results show nearly identical bias and uncertainty estimates suggesting that averaging the motions over random slip models produces as accurate a prediction at a site as a single motion computed using the "true" slip model which is determined from inverting actual recordings.

The rupture velocity is taken as depth independent at a value of 0.8 times the shear-wave velocity, generally at the depth of the dominant slip. This value is based on a number of studies of source rupture processes which also suggest that rupture velocity is non-uniform. To capture the effects of non-uniform rupture velocity, a random component is added through the randomized location of the subevents within each subfault. The radiation pattern is computed for each subfault, a random component added, and the RMS applied to the motions computed at the site when modeling an average horizontal component. To model individual horizontal components, the radiation pattern for each subfault is used to scale each subfault's contribution to the final summed motion.

The ground-motion time history at the receiver is computed by summing the contributions from each subfault associated with the closest Green function, transforming to the frequency domain, and convolving with the appropriate Green function spectrum. The locations of the Green functions are generally taken at center of each subfault for small subfaults or at a maximum separation of about 5 to 10 km for large subfaults. As a final step, the individual contributions associated with each Green function are summed in the frequency domain, multiplied by the RMS radiation pattern, and the resultant power spectrum at the site is computed. The appropriate duration used in the RVT computations for PGA, PGV, and oscillator response is computed by transforming the summed Fourier spectrum into the time domain and computing the 5 to 75% Arias intensity (Ou and Herrmann, 1990).

As with the point-source model, crustal response effects are accommodated through the amplification factor ($A(f)$) or by using vertically propagating shear waves through a vertically heterogeneous crustal structure. Soil nonlinearity is accommodated through the equivalent-linear approximation. Propagation path damping, through the $Q(f)$ model, is incorporated from each fault element to the site. Near-surface crustal damping is incorporated through the kappa operator (Equation A1). To model crustal propagation path effects, the raytracing method of Ou and Herrmann (1990) is applied from each subfault to the site.

Time histories may be computed in the process as well by simply adding a phase spectrum appropriate to the subevent earthquake. The phase spectrum can be extracted from a recording made at close distance to an earthquake of a size comparable to that of the subevent (generally M 5.0 to 6.5). Interestingly, the phase spectrum need not be from a recording in the region of interest (Silva et al., 1989). A recording in WNA (Western North America) can effectively be used to simulate motions appropriate to ENA (Eastern North America). Transforming the Fourier spectrum computed at the site into the time domain results in a computed time history which then includes all of the aspects of rupture propagation and source finiteness, as well as region specific propagation path and site effects.

References

- Abrahamson, N.A. and W.J. Silva (1997). "Empirical response spectral attenuation relations for shallow crustal earthquakes." *Seismological Research Lett.*, 68(1), 94-127.
- Beresnev, I.A. and G. M. Atkinson (2002). "Source parameters of earthquakes in Eastern and Western North America." *Bull. Seism. Soc. Am.*, 92(2), 695-710.
- Boore, D.M., W.B. Joyner, and T.E. Fumal (1997). "Equations for estimating horizontal response spectra and peak acceleration from Western North American earthquakes: A summary of recent work." *Seism. Res. Lett.* 68(1), 128-153.
- Boore, D.M., W.B. Joyner, and T.E. Fumal (1994). "Estimation of response spectra and peak accelerations from western North American earthquakes: and interim report. Part 2. *U.S. Geological Survey Open-File Rept.* 94-127.
- Boore, D.M. (1986). "Short-period P- and S-wave radiation from large earthquakes: implications for spectral scaling relations." *Bull. Seism. Soc. Am.*, 76(1) 43-64.
- Boore, D.M. (1983). "Stochastic simulation of high-frequency ground motions based on seismological models of the radiated spectra." *Bull. Seism. Soc. Am.*, 73(6), 1865-1894.
- Brune, J.N. (1971). "Correction." *J. Geophys. Res.* 76, 5002.
- Brune, J.N. (1970). "Tectonic stress and the spectra of seismic shear waves from earthquakes." *J. Geophys. Res.* 75, 4997-5009.
- Campbell, K.W. (1993) "Empirical prediction of near-source ground motion from large earthquakes." in V.K. Gaur, ed., *Proceedings, Intern'l Workshop on Earthquake Hazard and Large Dams in the Himalya*. INTACH, New Delhi, p. 93-103.
- Hartzell, S., A. Leeds, A. Frankel, and J. Michael (1996). "Site response for urban Los Angeles using aftershocks of the Northridge earthquake." *Bull. Seism. Soc. Am.*, 86(1B), S168-S192.

- Hartzell, S.H. (1978). "Earthquake aftershocks as Green's functions." *Geophys. Res. Letters*, 5, 1-4.
- Irikura, K. (1983). "Semi-empirical estimation of strong ground motions during large earthquakes." *Bull. Disaster Prevention Res. Inst.*, Kyoto Univ., 33, 63-104.
- Ou, G.B. and R.B. Herrmann (1990). "Estimation theory for strong ground motion." *Seism. Res. Letters*. 61.
- Schneider, J.F., W.J. Silva, and C.L. Stark (1993). "Ground motion model for the 1989 **M** 6.9 Loma Prieta earthquake including effects of source, path and site." *Earthquake Spectra*, 9(2), 251-287.
- Silva, W.J., N. Abrahamson, G. Toro, and C. Costantino (1997). "Description and validation of the stochastic ground motion model." Submitted to Brookhaven National Laboratory, Associated Universities, Inc. Upton, New York.
- Silva, W.J. and R. Darragh (1995). "Engineering characterization of earthquake strong ground motion recorded at rock sites." Palo Alto, Calif:Electric Power Research Institute, TR-102261.
- Silva, W.J. and C.L. Stark (1993) "Source, path, and site ground motion model for the 1989 **M** 6.9 Loma Prieta earthquake." CDMG draft final report.
- Silva, W. J., R. Darragh, C. Stark, I. Wong, J. C. Stepp, J. Schneider, and S-J. Chiou (1990). "A Methodology to Estimate Design Response Spectra in the Near-Source Region of Large Earthquakes Using the Band-Limited-White-Noise Ground Motion Model". *Procee. of the Fourth U.S. Conf. on Earthquake Engineering*, Palm Springs, California. 1, 487-494.
- Silva, W.J., R.B. Darragh, R.K. Green and F.T. Turcotte (1989). *Estimated Ground Motions for a new madrid Event*. U.S. Army Engineer Waterways Experiment Station, Wash., DC, Misc. Paper GL-89-17.
- Wald, D.J. (1996). "Slip history of the 1995 Kobe, Japan, earthquake determined from strong motion, teleseismic, and geodetic data." *J. of Physics of the Earth*, in press.
- Wald, D.J. and T.H. Heaton (1994). "Spatial and temporal distribution of slip for the 1992 Landers, California, earthquake." *Bull. Seism. Soc. Amer.*, 84(3), 668-691.
- Wells, D.L. and K.J. Coppersmith (1994). "New empirical relationships among magnitude, rupture length, rupture width, rupture area, and surface displacement." *Bull. Seism. Soc. Am.* 84(4), 974-1002.

Modeler 6: Dr. Paul Somerville et al., URS Corporation

The primary reference for the simulation procedure and its application to the 1994 Northridge earthquake is Somerville et al. (1996), pages S-116 through S-118. The application of the simulation procedure to the generation of ground motion time histories and response spectra at the sites of steel buildings in the FEMA/SAC Steel Project is described in Somerville et al. (1995).

The simulation procedure is based on rigorous seismological representations of the earthquake source and wave propagation. To simulate broadband time histories, a hybrid method is used which computes the ground motions separately in the short period and long period ranges and then combines them into a single time history (e.g. Somerville et al., 1996). The earthquake source is represented as a shear dislocation. The ground motion time history is calculated in the time domain using the elastodynamic representation theorem. In order to represent near-fault effects, ground motion simulations need to be based on the summation of complete Green's functions that contain near-, intermediate-, and far-field terms. This is done using the elastodynamic representation theorem, which states that the ground motion $U(t)$ can be calculated from the convolution of the slip time function $D(t)$ on the fault with the Green's function $G(t)$ for the appropriate distance and depth, integrated over the fault rupture surface (Aki and Richards, 1980):

$$U(t) = \sum D(t) * G(t)$$

At long periods, theoretical source models including the theoretical radiation pattern are used, while at short periods, empirical source functions derived from the recordings of small earthquakes are used that incorporate the radiation pattern empirically. For both procedures, the fault rupture plane is discretized into a number of equal size sub-fault regions. Fault asperities are represented by spatial variations in the amount of slip or slip velocity. The Green's functions are generated using frequency-wavenumber integration for long-periods and generalized rays for short periods.

References

- Aki, K. and P.G. Richards (1980). *Quantitative Seismology: Theory and Methods*. W.H. Freeman & Co.
- Somerville, P., C.K. Saikia, D. Wald, and R. Graves (1996). Implications of the Northridge earthquake for strong ground motions from thrust faults, *Bull. Seism. Soc. Am.*, 86, S115- S125.
- Somerville, P.G., R.W. Graves, and C.K. Saikia (1995a). Characterization of Ground Motions during the Northridge Earthquake of January 17, 1994. *Program to Reduce the Earthquake Hazards of Steel Moment Frame Buildings*, SAC Report 95-03.

Modeler 7: Dr. Yuehua Zeng

Based on fundamental earthquake source physics and seismic wave propagation, we have developed and improved a numerical simulation procedure to compute synthetic strong motion seismogram using a composite source model (Zeng et al., 1994). The method has been successful in generating realistic strong motion seismograms. The realism is demonstrated by comparing synthetic strong motions with observations from the recent California earthquakes at Landers, Loma Prieta (Su et al., 1994a,b) and Northridge (Zeng and Anderson, 1996; Anderson and Yu, 1996; Su et al., 1998), earthquakes in the eastern US (Ni et al., 1999) and earthquakes in Guerrero, Mexico (Zeng et al., 1994; Johnson, 1999), Turkey (Anderson et al., 2001) and India (Khatti et al., 1994; Zeng et al., 1995). We have also successfully applied the method for earthquake engineering applications to compute the ground motion of scenario earthquakes. During the process of continuing development, we have included scattering waves from small scale heterogeneity structure of the earth, site specific ground motion prediction using weak motion site amplification, and nonlinear soil response using the geotechnical engineering model. We have evaluated the numerical procedure for simulating near-fault long-period ground motions and rupture directivity, revisiting some of the above earthquake events, including Loma Prieta, Landers and Northridge. We also tested its ability to predict the near-fault ground motion observation from the 1979 Imperial Valley, California earthquake and the 1995 Kobe event (Zeng and Anderson, 2000).

The composite source model assumes a large earthquake is a superposition of smaller subevents that all break during the earthquake rupture processes. The number and radius of the subevents follow the Gutenberg and Richter frequency-magnitude relation given in form of a power law distribution of radii, $N(r) \sim r^{-p}$, where p is the fractal dimension. The source is kinematic, but this source description has the capability to generate realistic accelerograms with the proper frequency content (Zeng et al., 1994), and has a capability to predict ground motions (e.g. Anderson and Yu, 1996; Anderson et al., 2002). Also, it is possible, using a genetic algorithm, to find specific composite sources that are consistent with both the statistics and the phase of observed records (e.g. Zeng and Anderson, 1996). Several physical parameters of earthquake source (radiated energy, stress drops) can be expressed in terms of the composite source model parameters (Anderson, 1997). The high frequency radiation of the model is controlled by the subevent stress drops, maximum subevent radius and rupture velocity.

References

- Anderson, J., Graves, R., Zeng, Y., Somerville, P. (2002). Blind prediction of near-fault strong ground motions, AGU fall annual meeting, Abstract S72F-1349.
- Anderson, J. G., Y. Zeng and H. Sucuoglu (2001). Analysis of accelerations from the Dinar, Turkey earthquake, *Bull. Seis. Soc. Am.* **91**, 1433-1445.
- Anderson, J. G. (2000). Expected shape of regressions for ground-motion parameters on rock, *Bull. Seism. Soc. Am.* **90**, no. 6B, S43-S52.
- Anderson, J. G. (1997). Seismic energy and stress drop parameters for a composite source model. *Bull. Seism. Soc. Am.* **87**, 85-96.
- Anderson, J. G. and G. Yu (1996). Predictability of strong motions from the Northridge, California, earthquake, *Bull. Seism. Soc. Am.* No. 86, 1B, S100-S114.
- Johnson, M. (1999). Composite source model parameters for large earthquakes ($M > 5.0$) in the Mexican subduction zone, M. S. thesis, University of Nevada, Reno.

- Keaton, J. R. (2000). Synthetic seismograms for normal-faulting earthquakes using the composite source model, Report of the EERI-FEMA National Earthquake Hazards Reduction Program 1999 Professional Fellowship in Earthquake Engineering.
- Khatti, K. N., Y. Guang, J. G. Anderson, J. N. Brune and Y. Zeng (1994). Seismic hazard estimation using modelling of earthquake strong ground motions: A brief analysis of 1991 Uttarkashi earthquake, Himalaya and prognostication for a great earthquake in the region, *Current Science*, 67, 343-353.
- Lee, M. K. W. and W. D. L. Finn (1982). Dynamic effective stress response analysis of soil deposits with energy transmitting boundary including assessment of liquefaction potential, Rev., Dept. of Civil Eng., Soil Mechanics Series No. 38, the Univ. of British Columbia, Vancouver, Canada.
- Lee, Y., J. G. Anderson, and Y. Zeng (2000). Evaluation of empirical ground-motion relations in southern California, *Bull. Seism. Soc. Am.* **90**, no. 6B, S136–S148.
- Lucio, J. E. and R. J. Apsel (1983). On the Green's function for a layered half-space, part I, *Bull. Seism. Soc. Am.* 73, 909-929.
- Ni, S.-D., J. G. Anderson, Y. Zeng (1999). Comparison of strong ground motions from the 1988 Seguenay earthquake with the synthetic simulations using the composite source model, manuscript in progress.
- Su, Feng, Y. Zeng and J. G. Anderson (1994a). Simulation of the Loma Prieta earthquake strong ground motion using a composite source model, EOS, Trans. A.G.U., **75**, 44, p448.
- Su, F., Y. Zeng and J. G. Anderson (1994b). Simulation of Landers earthquake strong ground motion using a composite source model, *Seism. Res. Lett.*, **65**, p52.
- Su, F., J. G. Anderson and Y. Zeng (1998). Study of weak and strong motion including nonlinearity in the Northridge, California, earthquake sequence, *Bull. Seis. Soc. Am.* **88**, 1411-1425.
- Zeng, Y., J. G. Anderson and G. Yu (1994). A composite source model for computing realistic synthetic strong ground motions, *J. Res. Lett.*, **21**, 725-728.
- Zeng, Y., J. G. Anderson and Feng Su (1995). Subevent rake and scattering effects in realistic strong ground motion simulation, *Geophy. Res. Lett.*, **22**, 17-20.
- Zeng, Y. and J. G. Anderson (1996). A composite source modeling of the 1994 Northridge earthquake using Genetic Algorithm, *Bull. Seism. Soc. Am.* 86, No. 1B, 71-83.
- Zeng, Y. and J. G. Anderson (2000). Earthquake source and near-field directivity modeling of several large earthquakes, EERI Proceedings for the Sixth International Conference on Seismic Zonation.
- Zeng, Y. (2002). Final Technical Report on Validation of 1-D Numerical Simulation Procedures, Final Technical Report, PEER Project 1C02, Task 1: Earthquake ground motion, Seismological Lab, University of Nevada – Reno.